Since January 2020 Elsevier has created a COVID-19 resource centre with free information in English and Mandarin on the novel coronavirus COVID-19. The COVID-19 resource centre is hosted on Elsevier Connect, the company's public news and information website.

Research Article

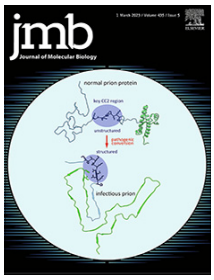

The Cytoplasmic Domain of the SARS-CoV-2 Envelope Protein Assembles into a β-Sheet Bundle in Lipid Bilayers

Aurelio J. Dregni [a†], Matthew J. McKay [a†], Wahyu Surya [b], Maria Queralt-Martin [c], João Medeiros-Silva [a], Harrison K. Wang [a], Vicente Aguilella [c], Jaume Torres [b] and Mei Hong [a*]

***a* - Department of Chemistry,** *Massachusetts Institute of Technology, 77 Massachusetts Avenue, Cambridge, MA 02139, United States*

***b* - School of Biological Sciences,** *Nanyang Technological University, 60 Nanyang Drive, Singapore 637551, Singapore*

***c* - Laboratory of Molecular Biophysics. Department of Physics. Universitat Jaume I. 12080 Castellón,** *Spain*

Correspondence to Mei Hong: *meihong@mit.edu (M. Hong)*

https://doi.org/10.1016/j.jmb.2023.167966

Edited by Ichio Shimada

Abstract

The severe acute respiratory syndrome coronavirus 2 (SARS-CoV-2) envelope (E) protein forms a pentameric ion channel in the lipid membrane of the endoplasmic reticulum Golgi intermediate compartment (ERGIC) of the infected cell. The cytoplasmic domain of E interacts with host proteins to cause virus pathogenicity and may also mediate virus assembly and budding. To understand the structural basis of these functions, here we investigate the conformation and dynamics of an E protein construct (residues 8–65) that encompasses the transmembrane domain and the majority of the cytoplasmic domain using solid-state NMR. ^{13}C and ^{15}N chemical shifts indicate that the cytoplasmic domain adopts a β-sheet-rich conformation that contains three β-strands separated by turns. The five subunits associate into an umbrella-shaped bundle that is attached to the transmembrane helices by a disordered loop. Water-edited NMR spectra indicate that the third β-strand at the C terminus of the protein is well hydrated, indicating that it is at the surface of the β-bundle. The structure of the cytoplasmic domain cannot be uniquely determined from the inter-residue correlations obtained here due to ambiguities in distinguishing intermolecular and intramolecular contacts for a compact pentameric assembly of this small domain. Instead, we present four structural topologies that are consistent with the measured inter-residue contacts. These data indicate that the cytoplasmic domain of the SARS-CoV-2 E protein has a strong propensity to adopt β-sheet conformations when the protein is present at high concentrations in lipid bilayers. The equilibrium between the β-strand conformation and the previously reported α-helical conformation may underlie the multiple functions of E in the host cell and in the virion.

Introduction

The SARS-CoV-2 is the causative agent of the COVID-19 pandemic, which claimed more than six million lives worldwide by the end of 2022. Although COVID vaccines are now widely available, antiviral treatments for infected individuals are still limited. One antiviral drug target is the envelope (E) protein, one of the three membrane proteins of the virus.[1] In SARS-CoV-1, the E protein consists of 76 amino acid residues: a short N-terminus spans residues 1–7, a transmembrane (TM) domain spans residues 8–38, and a C-terminal cytoplasmic domain (CTD)

encompasses residues 39–76. The protein localizes to the ERGIC compartment of infected cells, with the C-terminus oriented towards the cytoplasm.[2] E shows ion channel activities in three constructs: a transmembrane construct (ETM, residues 8–38),[3–9] a cytoplasmic-truncated construct (ETR, residues 8–65),[10] and full-length E (EFL).[11] The channel activity of E is a virulence factor: channel-inactivating mutations[3] in mouse-adapted SARS-CoV reduced lung edema and lowered the proinflammatory cytokine levels.[6] Ca^{2+} fluxes through the E channel are implicated in the pathogenicity of SARS-CoV-1 by activating the NOD-, LRR- and pyrin domain-containing protein 3 (NLRP3) inflammasomes.[5] This Ca^{2+} flux follows a three-orders-of-magnitude concentration gradient, from ~0.4 mM in the ERGIC lumen to ~0.1 μM in the cytoplasm.[12,13] The E protein of SARS-CoV-2 is highly homologous to the SARS-CoV counterpart, differing only by three residues and one deletion, all localized in the CTD. The TM sequence of the two proteins is identical. Therefore, the structure and function of these two proteins are likely similar.

The structure and stoichiometry of ETM have been investigated in a variety of membrane-mimetic environments. Gel electrophoresis and sedimentation equilibrium data in perfluoro-octanoic acid (PFO) and dodecylphosphocholine (DPC) detergents suggested that ETM forms pentamers.[9] This stoichiometry was recently firmly established for membrane-bound ETM using ^{19}F spin diffusion NMR,[14] where the protein was reconstituted in a cholesterol-containing ERGIC-mimetic lipid bilayer. Pentamer formation was also reported for ETR[10] and EFL[11,15] based on gel electrophoresis and sedimentation equilibrium data obtained from PFO, C14 betaine and DPC/sodium dodecylsulfate (SDS) micelles. Solution NMR data indicate that ETM is α-helical in DPC micelles,[16] and infrared spectra of DMPC bilayer-bound ETM showed amide I and II bands that are consistent with a helical conformation.[17] Recently, the high-resolution structure of SARS-CoV-2 ETM bound to ERGIC-mimetic membranes was determined using solid-state NMR (ssNMR).[18] ^{13}C and ^{15}N chemical shifts indicate that most of the TM domain is α-helical, but moderate helix non-ideality exists in the middle of the segment where three Phe residues are spaced every three residues apart.[19] Interhelical ^{13}C-^{15}N and ^{13}C-^{19}F correlations constrained the structure of the five-helix bundle, showing a channel with a pore diameter of 11–14 Å and a small helix tilt angle of ~10°. An asparagine (Asn) residue at position 15 is the main polar residue in the pore lumen, consistent with the observation that an N15A mutation abolished the ion channel activity.[3,8] This structure was solved at neutral pH in the absence of calcium ions, and likely represents a closed state of the channel.

While the TM domain of E mediates ion conduction, the CTD of E in SARS and other coronaviruses contains a C-terminal PDZ-binding motif (residues DLLV) that interacts with host proteins.[20–23] This host interaction is implicated in the pro-inflammatory cytokine release associated with SARS-CoV-2 infection, which causes severe tissue and organ damage.[24] For example, the cell-surface receptor TLR2 recognizes the E protein to initiate priming of the inflammasome.[25] E in other coronaviruses such as the infectious bronchitis virus also functions in virus assembly and budding,[26] potentially through interactions with the viral matrix (M) and spike (S) proteins.[1] To understand the mechanisms with which E carries out these diverse functions, it is important to elucidate the structure of the E cytoplasmic domain. For this purpose, ETR is a valuable model, as removal of the last ten residues of EFL has been shown to not affect the virulence of the virus in mice.[27]

To date, biophysical studies of the E CTD have yielded inconsistent information about the structure of this domain. Solution NMR studies of SARS-CoV ETR in SDS/DPC micelles showed that the CTD contains a single amphipathic helix, which spans residues 55–65.[10] But in LMPG (1-myristoyl-2-hydroxy-sn-glycero-3-phospho-(1′-rac-glycerol)) micelles, two amphipathic helices are reported, at residues 38–47 and 52–65.[28] In n-hexadecyl-phosphocholine (HPC) micelles, SARS-CoV-2 EFL shows chemical shifts and residual ^{15}N-^{1}H dipolar couplings that are consistent with a single helix spanning residues 52–60.[29] Thus, these data indicate that detergent-bound ETR and EFL are predominantly α-helical but the helices occur at variable positions in the amino acid sequence. Compared to these studies in detergent micelles, EFL and ETR in lipid bilayers and short cytoplasmic peptides in solution have been reported to adopt β-sheet conformations. A synthetic peptide corresponding to residues 46–60 of the CTD has a high tendency to aggregate in solution and absorbs at 1635 cm^{-1} in Fourier-transform infrared (FT-IR) spectra,[10,30] indicating β-sheet formation. Similarly, a nine-residue peptide corresponding to residues 55–63 of the CTD assembles into amyloid fibrils in solution.[31] FT-IR spectra of DMPC-bound EFL show a shoulder at 1635 cm^{-1}, consistent with β-sheet conformation.[10] The same peak is reported for ERGIC membrane-bound SARS-CoV-2 EFL and ETR.[15] Therefore, these data suggest a significant propensity of the CTD to form β-sheet conformations under certain conditions.

To clarify and investigate the structure of the E CTD in a residue-specific manner, here we employ magic-angle-spinning (MAS) ssNMR spectroscopy. We reconstituted SARS-CoV-2 ETR into DMPC/DMPG membranes and measured its ^{13}C and ^{15}N chemical shifts and inter-residue contacts using two-dimensional (2D) and three-dimensional (3D) correlation experiments. The chemical shifts and distance constraints indicate that the CTD folds into a

triple-stranded β-sheet, which oligomerizes into an umbrella-shaped β-bundle outside the membrane. This β-sheet structure coexists with the TM helices, indicating a clear separation of the ion channel function of E from its host-interaction and virus assembly functions.

Materials and methods

Cloning, expression and purification of SARS-CoV-2 ETR (residues 8–65)

The SARS-CoV-2 ETR (^{8}ETG TLIVNSVLLF LAFVVFLLVT LAILTALRLA AYAANIVNVS LVKPSFYVYS RVKNL^{65}) spans residues 8–65 of the full-length protein and contains three Cys to Ala mutations, C40A, C43A, and C44A. The construct was derived from a SARS-CoV ETR construct in the pNIC28-Bsa4 plasmid[10,32] by introducing two changes at T55S and V56F, which are the only two residues that differ between SARS-CoV and SARS-CoV-2 E proteins between residues 1–68. The DNA sequence was confirmed by Sanger sequencing (Axil Scientific, Singapore). The plasmid was transformed into competent *E. coli* BL21 CodonPlus (DE3) pLysS cells (Agilent) for protein expression and then kept at −80 °C as a glycerol stock.

A 50 mL LB starter culture was inoculated from the glycerol stock and grown overnight with shaking at 37 °C. This starter culture was used to inoculate 0.8 L of ZYM-505 media[33] at an inoculum ratio of 1:100. The culture was grown in a 1 L fermenter (Winpact, USA) at 37 °C with the dissolved oxygen level maintained at 40% by controlling the agitation (up to 900 rpm), aeration (up to 1 vessel volume per minute), and oxygen supplementation, cascaded in the listed order. After 6 h, cells were collected by centrifugation at 7500*g* for 8 min at 30 °C. The pellet was resuspended in 0.8 L M9 media for high-cell density culture[34] containing 0.1% w/v NH_4Cl and 0.4% w/v glucose. The culture was transferred into a sterile 1 L fermenter vessel and further grown under the same condition as before centrifugation. After 1 hour, the temperature was lowered to 18 °C, the media was supplemented with 0.1% w/v NH_4Cl and 0.4% w/v glucose, and protein expression was induced by adding 0.5 mM IPTG. Expression proceeded overnight, then the cells were harvested the next day by centrifugation at 7500*g* for 10 min at 4 °C. The pellets were flash-frozen with liquid nitrogen and kept at −80 °C until used. Isotopically labeled ETR samples were produced by substituting unlabeled NH_4Cl and glucose with ^{15}N-labeled NH_4Cl and uniformly ^{13}C-labeled glucose (Cambridge Isotope Laboratories). Three isotopically labeled proteins were produced: ^{15}N-labeled ETR, ^{13}C-labeled ETR, and doubly ^{15}N, ^{13}C-labeled ETR.

Frozen cell pellets were resuspended, lysed, clarified, and applied to Ni-NTA resin for purification by affinity column chromatography as described previously.[10] The only change is that the elution buffer in the current study contained 0.1% w/v of N,N-dimethyldodecylamine N-oxide (LDAO). Following elution, the His_6 tag was cleaved by adding 1:10 mol/mol TEV protease in the presence of 1 mM ethylenediaminetetraacetic acid (EDTA) and 5 mM dithiothreitol (DTT). The reaction mixture was agitated by rolling at 4°C for 64 hours, then precipitated using trichloroacetic acid, and lyophilized. The lyophilized powder was dissolved in 5% v/v TFA in acetonitrile and injected into a Phenomenex Jupiter C18 column (10 μm particle size, 250 × 21.2 mm). The cleaved protein was fractionated from uncleaved protein using a linear gradient of isopropanol: acetonitrile (4:1 v/v with 0.1% v/v TFA) on a Shimadzu Prominence HPLC system. The identity and purity of the fractions was assessed by SDS-PAGE and MALDI-TOF mass spectrometry. The solvent was removed from pooled fractions in a vacuum concentrator, then the protein was lyophilized in the presence of 1 mM HCl. The isotopic labeling level was found to be close to 100% based on the MS spectra. The final ETR yield ranged from 5–10 mg per liter of M9 culture.

Membrane sample preparation for solid-state NMR experiments

Five membrane samples were prepared for this study. Three samples contained uniformly ^{13}C, ^{15}N-labeled ETR, one contained ^{13}C-labeled ETR, and one contained a 1: 1 mixture of ^{13}C-labeled and ^{15}N-labeled ETR. All membrane samples were prepared in a pH 7.5 Tris buffer (20 mM Tris-HCl, 5 mM NaCl, 2 mM EDTA and 0.2 mM NaN_3).

All lipids were purchased from Avanti Polar Lipids. Most ssNMR spectra were measured on ETR bound to a dimyristoyl-phosphatidylcholine (DMPC):dimyristoyl-phosphoglycerol (DMPG) (4:1) membrane. This membrane is denoted as DMPX in this work. A second lipid mixture is an ERGIC-mimetic membrane that consists of 1-palmitoyl-2-oleoyl-glycero-3-phosphocholine (POPC), 1-palmitoyl-2-oleoyl-sn-glycero-3-phosphoethanolamine (POPE), bovine phosphatidylinositol (PI), 1-palmitoyl-2-oleoyl-sn-glycero-3-phospho-L-serine (POPS), and cholesterol (Chol) at a molar ratio of 45:20:13:7:15.[18] Thus, both membranes have similar negative charge fractions of 20–24 mol%, excluding cholesterol. Most NMR samples used a protein/lipid molar ratio (P/L) of 1:20, where the concentrations of phospholipids but not cholesterol are considered. ETR (residues 8–65) has an isoelectric point of 9.8 and an estimated charge of +2.9 at pH 7.0. Thus, at the P/L of 1:20, the protein and membrane charges are approximately balanced.

To assess spectral resolution and sensitivity, we prepared DMPX and ERGIC membrane samples that contained only 2 mg ^{13}C, ^{15}N-labeled ETR. We found similar chemical shifts between the two samples and higher spectral resolution for the

DMPX sample. Therefore, for 3D correlation experiments that require extensive signal averaging, we used the DMPX-bound ETR. About 5 mg ^{13}C, ^{15}N-labeled ETR was used for these resonance assignment experiments. Intermolecular 2D NHHC and long-mixing 2D CC experiments were conducted on a sample containing 4 mg each of ^{13}C-labeled ETR and ^{15}N-labeled ETR. This mixture was reconstituted into the DMPX membrane at P/L 1: 15 to obtain sufficient spectral sensitivity.

Proteoliposomes of ETR were prepared using an organic-phase mixing protocol. Care was taken to ensure that the protein was fully dissolved throughout the sample preparation process, since ETR has a propensity for aggregation. Lipids were first dissolved in 400 μL chloroform, then chloroform was removed under a gentle stream of nitrogen gas, and the mixture was dried overnight under vacuum at room temperature to obtain a clear film. We dissolved 1 mg aliquots of lyophilized ETR in 0.5 mL trifluoroethanol (TFE). The solubility of ETR in TFE was ~1 mg/250 μL, thus the solution was free of aggregates. The protein solution was added to the dry lipid film, mixed by pipetting up and down, then vortexed. TFE was then removed with nitrogen gas, and the mixture was dried overnight under vacuum at room temperature. The mixed ^{13}C-labeled and ^{15}N-labeled ETR was prepared similarly. Here, the appropriate amount of lipids was dissolved in 400 μL chloroform, separated into four 100-μL aliquots and dried. 1 mg aliquots of ^{13}C-labeled or ^{15}N-labeled ETR were separately dissolved in 0.5 mL TFE, then combined and added to one of the four aliquots of dry lipids. This procedure was repeated until all 8 mg of ETR were mixed with the lipids.

For all samples, the dry proteoliposome film was resuspended in 3 mL of buffer (20 mM Tris pH 7.5, 5 mM NaCl, 2 mM EDTA, 0.2 mM NaN_3) by bath sonication at 25°C for at least 30 min until the suspension became homogeneous. This sonication step was not necessary for ETM but was found to be important for obtaining homogeneous suspensions of ETR.[18] The solution was subjected to nine freeze–thaw cycles between liquid nitrogen and a 42 °C water bath. The resulting proteoliposome solution appeared homogeneous and translucent. The solution was ultracentrifuged for 2 hours at 164,000*g* and 4 °C to obtain a membrane pellet. This pellet was placed in a desiccator until it reached a hydration level of 40% (w/w), before it was spun into an MAS rotor for ssNMR experiments.

Measurements of ETR ion channel activities in lipid bilayers

Planar lipid bilayers were formed by apposition of two lipid monolayers on a 15 μm-thick Teflon partition with a 100 μm diameter orifice that separated two identical chambers.[35,36] All lipids were purchased from Avanti Polar Lipids (Alabaster, AL). A lipid mixture that mimics the ERGIC membranes contained dioleoyl-phosphatidylcholine (DOPC), dioleoyl-phosphatidylethanolamine (DOPE), dioleoyl-phosphatidylserine (DOPS), dioleoyl-phosphatidylinositol (DOPI), and cholesterol (Chol) with a DOPC: DOPE: DOPI: DOPS: Chol molar ratio of 45:20:13:7:15. Prior to addition to the chamber, lipids dissolved in chloroform were mixed at the desired ratio, then chloroform was evaporated under an Argon constant flow followed by pentane addition. The orifice was pretreated with a 1% solution of hexadecane in pentane. Aqueous solutions were 100 mM $CaCl_2$ at pH 6.0. The pH of the solution was controlled using a GLP22 pH meter (Crison). All measurements were performed at room temperature (23 ± 1 °C).

ETR (residues 8–65) was inserted into the ERGIC-mimetic membrane by adding 0.5–1.0 μl of a 2.5 mg/mL ETR solution in acetonitrile: isopropanol (40:60) to one side of the chamber (*cis* side). An electrical potential was applied using Ag/AgCl electrodes in 2 M KCl, 1.5% agarose bridges assembled within standard 250 μL pipette tips. The potential was defined as positive when it was higher on the *cis* side, whereas the *trans* side was set to ground. An Axopatch 200B amplifier (Molecular Devices, Sunnyvale, CA) in the voltage-clamp mode was used to measure the current and the applied potential. Data were filtered by an integrated low pass 8-pole Bessel filter at 10 kHz, saved at a sampling frequency of 50 kHz with a Digidata 1440A (Molecular Devices, Sunnyvale, CA) and analyzed using the pClamp 10.7 software (Molecular Devices, Sunnyvale, CA). For visualization, current traces were digitally filtered at 500 Hz using a low-pass Bessel (8-pole) filter. The chamber and the headstage were isolated from external noise sources with a double metal screen (Amuneal Manufacturing Corp., Philadelphia, PA). Channel conductance was obtained from currents measured under an applied potential of +100 mV in symmetrical salt solutions. Current was calculated from a single-Gaussian fitting of the histogram of current jump amplitudes generated after addition of ETR to the chamber. The standard deviation of the data corresponds to the sigma obtained from the Gaussian fit. The histogram contains events from a minimum of 3 independent experiments.

Solid-state NMR experiments

All ssNMR spectra were measured on a Bruker Avance II 800 MHz (18.8 T) spectrometer using a Black Fox 3.2 mm MAS probe. The MAS frequencies were 14 kHz or 10.5 kHz. Typical radiofrequency (RF) field strengths were 50–91 kHz for ^{1}H, 50–63 kHz for ^{13}C, and 33–42 kHz for ^{15}N. Sample temperatures were estimated from the water ^{1}H chemical shift δ_{water} in ppm

using the equation $T_{sample} = (7.762\text{-}\delta_{water}) \times 96.9$ K .[37] ^{13}C chemical shifts are reported on the tetramethylsilane scale using the adamantane CH_2 chemical shift at 38.48 ppm as an external standard. ^{15}N chemical shifts are reported on the liquid ammonia scale using the N-acetylvaline peak at 122.00 ppm as an external standard.

2D ^{13}C–^{13}C correlation (CC) experiments were conducted using COmbined $R2^{v}_{n}$-Driven (CORD) mixing[38] for ^{13}C spin diffusion. 2D ^{15}N-^{13}C correlation (NC) experiments and 3D NCACX, NCOCX and CONCA[39] correlation experiments used SPECtrally Induced Filtering In Combination with Cross Polarization (SPECIFIC-CP)[40] for ^{15}N-^{13}C polarization transfer. Water-edited 2D NC spectra[41,42] were measured using ^{1}H mixing times of 9 ms and 100 ms. The experiment selects the water ^{1}H magnetization using a Hahn echo containing a Gaussian 180° pulse of 0.95 ms, then transfers this magnetization to protein protons for detection through ^{13}C. An Hγ-edited 2D CC spectrum was measured using the same pulse sequence, except that the ^{1}H carrier frequency was placed at 3.264 ppm to be on resonance with the DMPC Hγ peak. The Gaussian 180° pulse length for this Hγ selection was 2.86 ms and the ^{1}H mixing time was 25 ms. 2D ^{1}H–^{13}C heteronuclear correlation (HETCOR) spectra[43,44] were measured using a ^{1}H spin diffusion mixing time of 4 ms and a total ^{1}H T_2 filter time of 1.43 ms, which corresponded to 20 rotor periods under 14 kHz MAS. 2D NHHC correlation spectra[45] for obtaining intermolecular correlations were measured using a ^{1}H mixing time of 0.5 ms. Additional parameters for the solid-state NMR experiments are given in Table S1.

NMR spectra were processed using the Bruker TopSpin software, and chemical shifts were assigned using the Sparky software.[46] Backbone (ϕ, ψ) torsion angles were calculated using the TALOS-N software[47] after converting the ^{13}C chemical shifts to the DSS scale. 2D hydration maps of water-edited 2D NC spectra were obtained by dividing the intensities of the 9 ms spectrum (S) by the 100 ms spectrum (S_0) using a Python script.[42,48] The intensities of the two spectra were read using the NMRglue package.[49] Spectral noise was filtered by setting signals lower than 3.5 times the noise level to zero for the 9 ms spectrum and to a large number (900,000) for the 100 ms spectrum. This 2D hydration map reflects the water accessibilities of the protein residues.

XPLOR-NIH structure calculations

We calculated the ETR structure using the XPLOR-NIH software[50] hosted on the NMRbox.[51] For each simulated annealing run, five extended monomers (residues 8–65) were placed in a fivefold symmetric geometry, with each monomer parallel to the C_5 axis of the pentamer and the center of each monomer being 20 Å from the symmetry axis. TM residues E8-R38 were included in the structure calculation. However, due to the scarcity of interhelical contacts for these residues in ETR, we used previously reported interhelical ^{15}N-^{13}C contacts obtained from the NHHC spectra of the ETM peptide.[18] The TM helices and their inter-residue contacts are not necessary for constraining the CTD structure; however, their inclusion in simulated annealing prevented undesirable entanglement of the initial CTD random coils, which resulted in structures with poorly folded conformations.

A total of 10,000 independent simulated annealing runs were performed with 5,000 steps of torsion angle dynamics at 5,000 K, followed by annealing to 20 K in decrements of 10 K with 100 steps at each temperature. Energy minimization was subsequently carried out in torsion angle and then Cartesian coordinates. The five monomers were restrained to be identical using the non-crystallographic symmetry term PosDiffPot and the translational symmetry term DistSymmPot, with scales of 1000 and 100, respectively. Chemical-shift constrained (ϕ, ψ) torsion angles were implemented with the dihedral angle restraint term CDIH, with scale ramped from 50 to 500. Due to ambiguity in resonance assignment, we excluded the TALOS predictions for residues 8–11 and 37–44. Torsion angle ranges were set to the higher value between twice the TALOS-N predicted uncertainty and 20°. Experimentally measured distance constraints were included using the NOE potential, which was set to “soft”, with a scale ramped from 2 to 30. Distance upper limits were set to 9.0 Å for the NHHC restraints measured with 0.5 ms ^{1}H mixing[45] and 7.0 Å for the CC restraints measured with 250 ms mixing.[18] Implicit hydrogen bonds were included with the HBDB potential. Standard bond angles and lengths were set with terms BOND, ANGL and IMPR, and the nonbonded potential was implemented with XPLOR’s VDW term.

Spin diffusion contacts were applied to each of the five monomers: intermolecular contacts could be with either the molecule on the left or on the right of the source molecule, so they were set to have a twofold directional ambiguity in the structure calculation. Contacts that have unknown intramolecular or intermolecular origins were set to have threefold ambiguity, contacting the molecule on the left, on the right, or to the same molecule. NHHC contacts are unambiguously intermolecular because they are between ^{15}N-labeled monomers and ^{13}C-labeled monomers. Contacts observed in the 250 ms 2D CC spectrum of the 1:1 diluted sample were sorted by the intensity ratios (S/S_0) between the diluted and undiluted spectra into intramolecular ($S/S_0 > 0.8$), intermolecular ($S/S_0 < 0.6$), or unknown ($0.6 < S/S_0 < 0.8$). The intensity cutoffs were validated by the fact that all intra-residue contacts have intensity ratios of 0.8–1.2 between diluted and undiluted samples. Contacts from all other spectra were set to have

unknown intramolecular or intermolecular origins, with the exception of sequential contacts, which were assumed to be intramolecular. Table S3 summarizes the number of spin diffusion contacts of different types, and Table S4 lists all contacts used for structure calculation.

The 10,000 simulated structures were sorted by total energy. The structures did not converge. Thus we sorted the topology of the 20 lowest energy structures based on the relative orientation of the three β-strands (residues 45–65). Four topologies were identified. We took the lowest energy structure of a given topology as representative of that class, and measured the pairwise all-atom RMSD from every other structure with the same topology to the class representative. This analysis showed that the all-atom RMSD within each topology class is always less than 4 Å for residues 45–65. The next 80 lowest energy structures were also characterized for topology and RMSD to the four classes, and all but 22 out of 80 structures fit into one of the four classes with an RMSD of less than 4 Å. The all-atom RMSDs between different topologies range from 3 to 15 Å. Most of the remaining models showed putatively unphysical threading of one monomer through loops in the adjacent monomers. Images of the ETR structural models were generated in PyMOL v2.3.4.

Results

In this study, we investigate the SARS-CoV-2 E cytoplasmic structure using the ETR construct (residues 8–65) instead of EFL, because EFL is prone to aggregation[30] and mouse data show that removal of the last ten residues of the full-length protein did not reduce the virulence of the virus.[27] We expressed ETR as a His-tagged fusion protein, which was then cleaved and purified using affinity chromatography and HPLC. The HPLC chromatogram and SDS-PAGE (Figure S1) indicate high purity of the protein for structural analysis by ssNMR.

Ion channel activity of ETR

To verify the ion channel activities of ETR and investigate whether they differ from those of ETM, we measured the conductance of ETR in an ERGIC-mimetic lipid membrane. In 100 mM $CaCl_2$ at pH 6, ETR exhibits both single and multi-channel insertion events and conductance jumps, with variable conductance and stability (Figure 1(a)). The most probable conductance is 103 pS, which is similar to the most probable conductance of 110 ± 40 pS for ETM under similar conditions.[5,8] The ETR conductance is more variable than ETM, as shown by a larger standard deviation of 71 pS. We attribute this variability to the destabilizing effects of the cytoplasmic residues to the TM helices. Overall, these data indicate that ETR forms functional channels in ERGIC-mimetic lipid membranes.

Backbone conformation of ETR in lipid bilayers

We measured most ssNMR spectra of ETR in the DMPX membrane. One-dimensional (1D) ^{13}C NMR spectra show relatively resolved signals, whose intensities are twofold higher in the gel phase of the DMPX membrane at 263 K compared to the liquid-crystalline phase at 303 K (Figure 2(a)). This temperature dependence indicates that ETR is partially mobile in the liquid-crystalline membrane. 2D NC and CC spectra show many α-helical chemical shifts, as expected for the TM domain. In addition, we also observed β-sheet signals at characteristic chemical shifts of Ser, Val and Ile residues (Figure 2(b, c)). These β-sheet chemical shifts are absent from the ETM spectra. The ^{13}C and ^{15}N linewidths of the β-sheet signals are 0.6–0.8 ppm and 1.0–1.3 ppm, respectively, indicating high conformational homogeneity. In comparison, the α-helical signals have linewidths of 1.0–1.2 ppm for ^{13}C and 1.5–2.0 ppm for ^{15}N. These linewidths are broader than the α-helical signals of ETM, even though the average chemical shifts remain the same. Therefore, the TM domain becomes more disordered in the presence of the CTD. Given these broader linewidths, and because the TM helix structure is known from recent studies of ETM,[14,18,19] we focus on structure determination of the CTD in this study.

To assess if the conformational disorder of ETR is sensitive to the membrane environment, we compared the spectra of ETR in the DMPX membrane versus the ERGIC membrane (Figure S2(a, b)). The ^{13}C and ^{15}N chemical shifts are identical, but the linewidths are larger in the ERGIC membrane, suggesting that the cholesterol- and PI-containing ERGIC lipid mixture increases the protein disorder without affecting the average conformation. Thus, we used the DMPX membrane for 3D correlation experiments. To assess if the β-sheet conformation of the CTD is a result of high protein concentrations or is intrinsic to the amino acid sequence, we reduced the P/L ratio from 1:20 to 1:60. The diluted sample shows a nearly identical 2D CC spectrum as the 1:20 sample, with β-sheet chemical shifts coexisting with α-helical signals (Figure S2(c)). Thus, within the P/L range of 1:20 to 1:60, the β-sheet conformation of the CTD is intrinsic to membrane-bound ETR.

To determine the residue-specific conformation of ETR, we resolved and assigned the ^{13}C and ^{15}N chemical shifts using 3D NCACX, NCOCX and CONCA correlation experiments. Figure 3 shows representative strips for TM and CTD residues. Well-resolved signals are observed for both domains, which allowed sequential assignment of

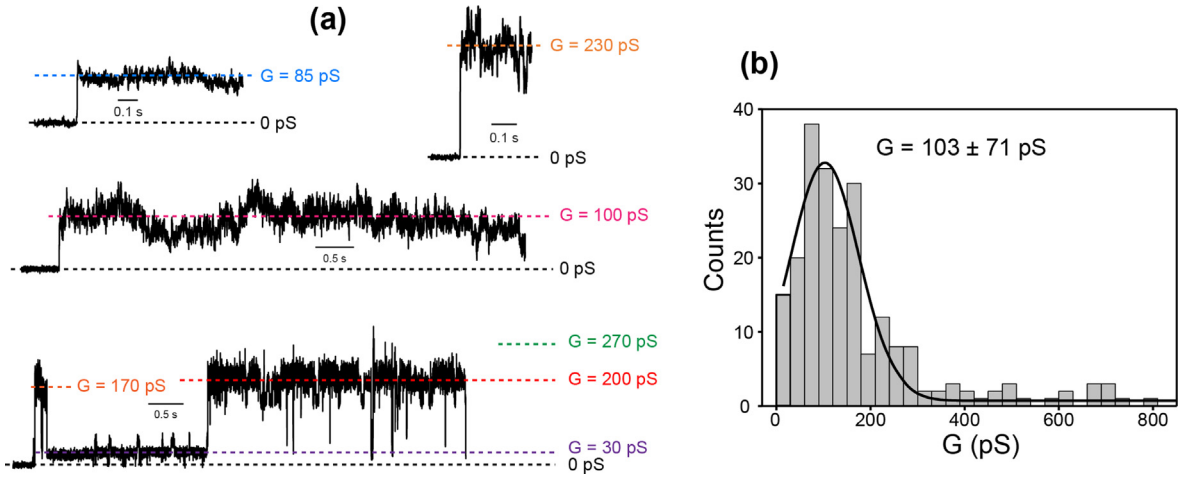

Figure 1. Membrane-bound ETR conducts ions across ERGIC-mimetic lipid bilayers. (a) Representative current recordings (reported in pS) show channel opening events with variable durations and conductance. The measurements were conducted in solutions containing 100 mM $CaCl_2$. Applied voltage was +100 mV. (b) Histogram of conductance jumps of ETR in 100 mM $CaCl_2$ solution under +100 mV applied voltage. Solid line indicates Gaussian fitting of the histogram, which yields a most probable G value of 103 pS with a standard deviation of 71 pS. The total number of events was 240.

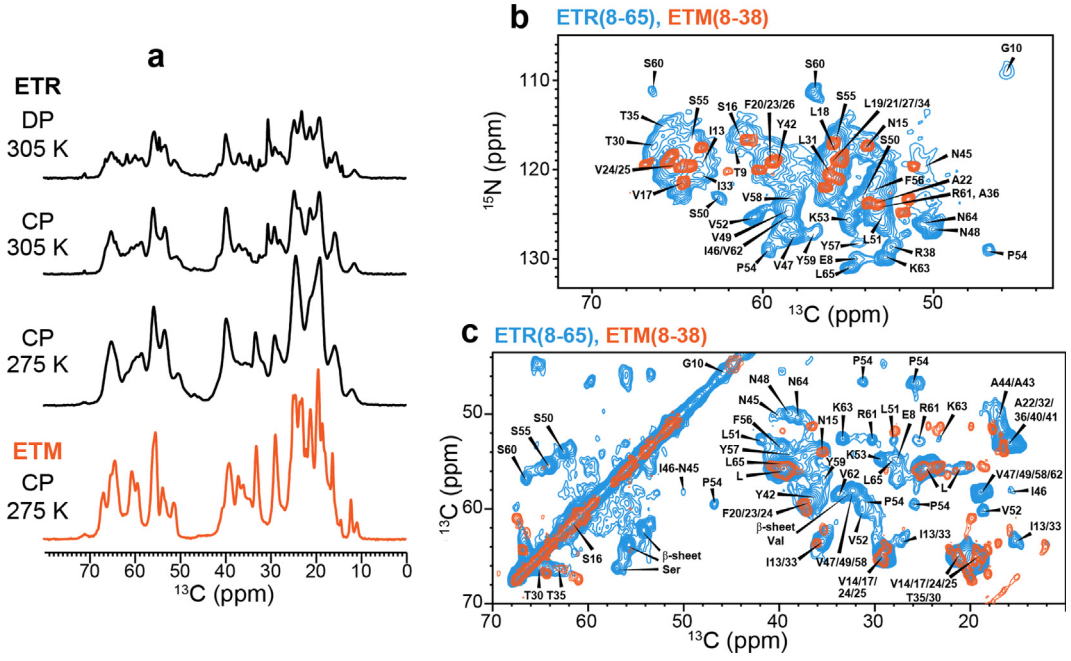

Figure 2. 1D and 2D NMR spectra of ETR in the DMPC: DMPG membrane. (a) ^{13}C cross-polarization (CP) and direct-polarization (DP) spectra of ETR (black) at 305 K and 275 K. The CP spectra preferentially detect immobilized residues whereas the DP spectrum preferentially detects mobile residues. The CP spectrum of ETM (orange) is also shown for comparison. (b) 2D NC spectrum of ETR (blue) measured at 305 K, overlaid with the ETM spectrum (orange) for comparison. ETR assignments obtained from 3D correlation spectra are indicated. (c) 2D CC spectrum of ETR (blue) measured at 305 K, overlaid with the ETM spectrum (orange). β-sheet chemical shifts are observed for residues such as Ser and Val, which are absent in the ETM spectrum.

46 out of the 58 residues (Table S2). α-helical chemical shifts are observed for residues from the N-terminus to A36, whereas β-sheet chemical shifts are observed for residues N45 to L65 (Figure 4(a)). The TM residues exhibit similar chemical shifts as in ETM, except for residues 8–

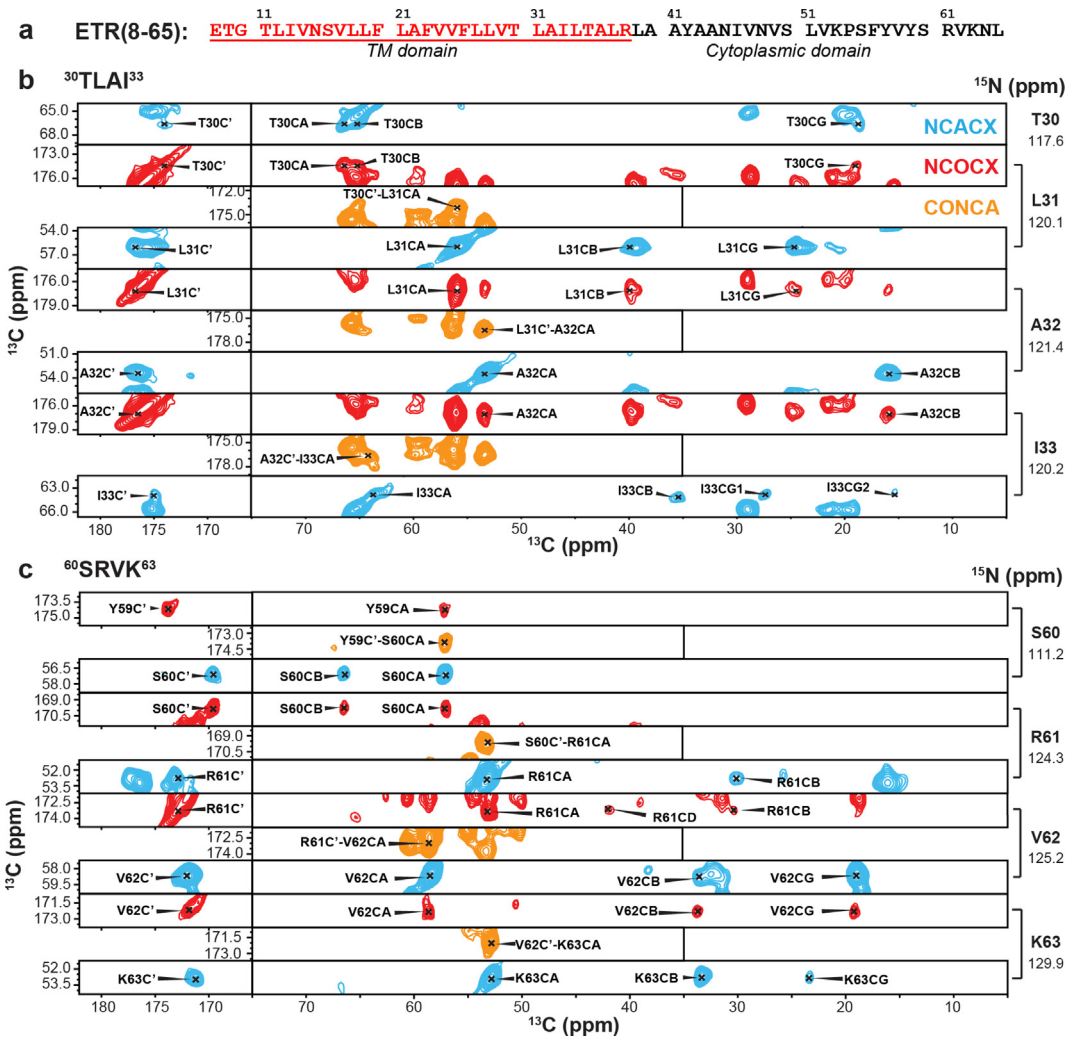

Figure 3. Resonance assignment of ETR bound to DMPC: DMPG membranes. (a) Amino acid sequence of ETR (residues 8–65). The TM residues are colored in red. (b, c) Representative 3D strips of the NCACX, NCOCX and CONCA spectra for (b) TM residues ^{30}TLAI^{33} and (c) cytoplasmic residues ^{60}SRVK^{63}.

13 and 34–38 (Figure 4(b)).[18] The (ϕ, ψ) torsion angles predicted from these chemical shifts indicate that residues 12–36 form the α-helical core of ETR, whereas residues 45–64 contain three β-strands (Figure 4(c)). The β1 strand extends from N45 to V52, β2 from S55 to V58, and β3 from R61 to N64. These three β-strands are separated by the Pro-containing ^{53}KP^{54} and by ^{59}YS^{60}.

Membrane topology of the cytoplasmic domain

To probe the membrane topology of the triple-stranded CTD, we measured the depth of insertion of ETR in the DMPX membrane using a 2D ^{1}H–^{13}C HETCOR experiment.[52] The experiment correlates the lipid and water ^{1}H chemical shifts with the protein ^{13}C signals after a ^{1}H mixing period. Even with a short mixing time of 4 ms, the 2D spectrum already exhibits extensive correlation peaks between the lipid chain protons at 1.3 ppm and the α-helical chemical shifts of Val, Leu and Ala residues. This indicates that the α-helical TM residues are well inserted into the membrane (Figure 5(a, b)). The water ^{1}H cross section at 4.7 ppm shows many cross peaks with β-sheet signals of the cytoplasmic residues such as S60 and S55 Cβ, P54 Cδ, and F56 and Tyr aromatic carbons. In the aromatic region of the HETCOR spectrum, F20, F23 and F26 in the TM domain show cross peaks with the lipid chain protons whereas the cytoplasmic F56 exhibits cross peaks with water. Strong cross peaks between Tyr and water are also observed. There are three Tyr residues in ETR, all located in the CTD, thus these Tyr-water cross peaks indicate the high water accessibility of the CTD. These Phe and Tyr residues have partially resolved ^{13}C chemical shifts (Figure S3), which make them infor-

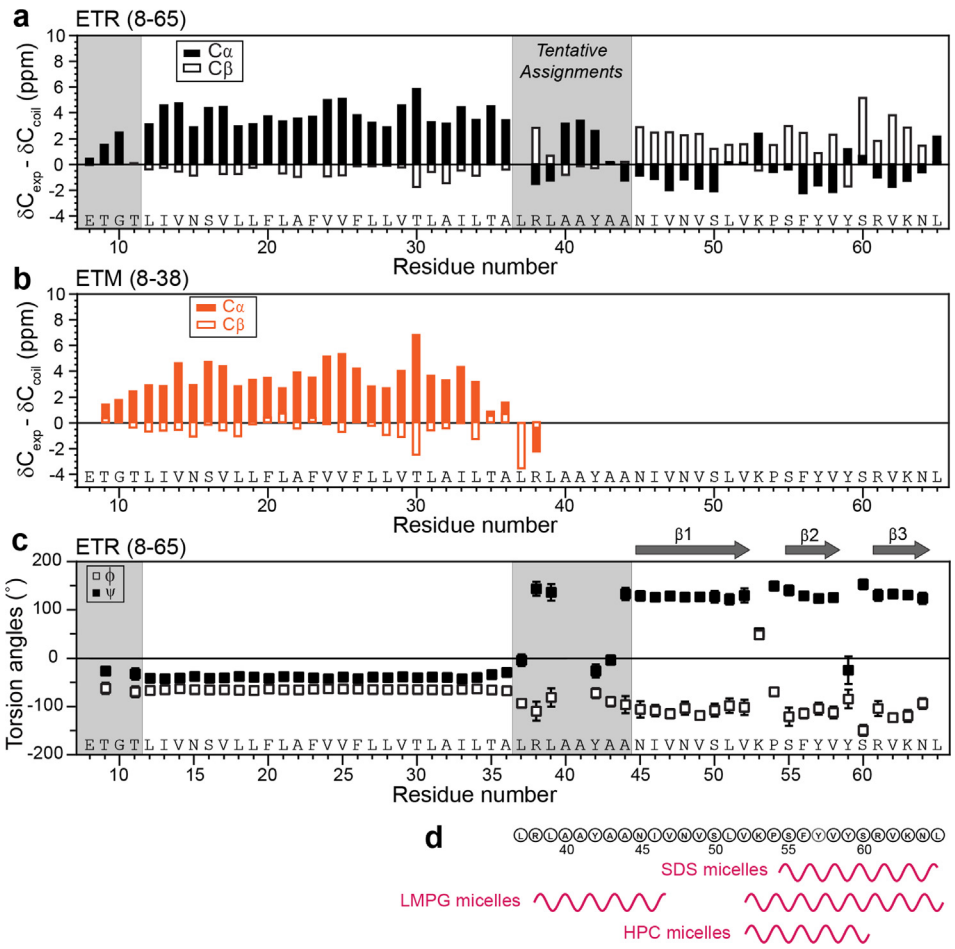

Figure 4. Secondary structure of membrane-bound ETR obtained from ^{13}C and ^{15}N chemical shifts. (a) Cα and Cβ secondary chemical shifts. Most CTD residues show negative Cα and positive Cβ secondary shifts, indicating a β-sheet conformation. Residues 8–11 and 37–44 are tentatively assigned. (b) Cα and Cβ secondary chemical shifts of ETM.[18] (c) (φ, ψ) torsion angles of ETR. Membrane-bound E shows three β-strands in the CTD, separated by K53-P54 and Y59-S60. (d) Comparison of the secondary structures of the E CTD in different membrane-mimetic environments.[16,28,29] Detergent-bound E has α-helical CTD conformations.

mative probes of the differential depths of insertion and water exposure of the TM and cytoplasmic domains. Together, these data indicate that the β-sheet CTD is well exposed to water while the middle of the TM domain is deeply inserted into the membrane.

The lipid headgroup Hγ cross section at 3.26 ppm in the HETCOR spectrum provided additional information about the membrane topology of ETR. Cross peaks with G10, A43/A44/N45, and a Tyr sidechain are observed. The most likely Tyr that gives rise to this cross peak is Y42, since Y57 and Y59 are adjacent to F56 and other CTD residues and are thus most likely well hydrated. These results indicate that the linker between the TM and cytoplasmic domains lies near the membrane surface. Other cross peaks at both α-helical and β-sheet chemical shifts are also detected. To better resolve the signals of these membrane-surface residues, we conducted a Hγ-edited 2D CC experiment, which selectively transfers the Hγ magnetization to protein protons for detection through ^{13}C (Figure S4). With a ^{1}H mixing time of 25 ms, the Hγ-edited 2D CC spectrum exhibited residual intensities for α-helical Val and Leu residues, β-sheet CTD residues such as V47 or V49, and Ala and Tyr residues in the linker region. Intensity analysis indicates that the α-helical Val and Leu residues have low Hγ-transferred intensities while the ^{42}YAA^{44} segment has high Hγ-transferred intensities. However, this Hγ transfer reduces the spectral sensitivity by 100-fold compared to the unedited 2D CC experiment, thus the intensity differences are not significantly larger than the experimental uncertainty. Thus, we only consider the 4 ms ^{1}H–^{13}C HETCOR spectrum in evaluating the relative merit of the various membrane topologies obtained from the structure calculation.

Complementing the 2D ^{1}H–^{13}C HETCOR spectrum, we also measured water-edited 2D NC spectra to determine the water-accessible

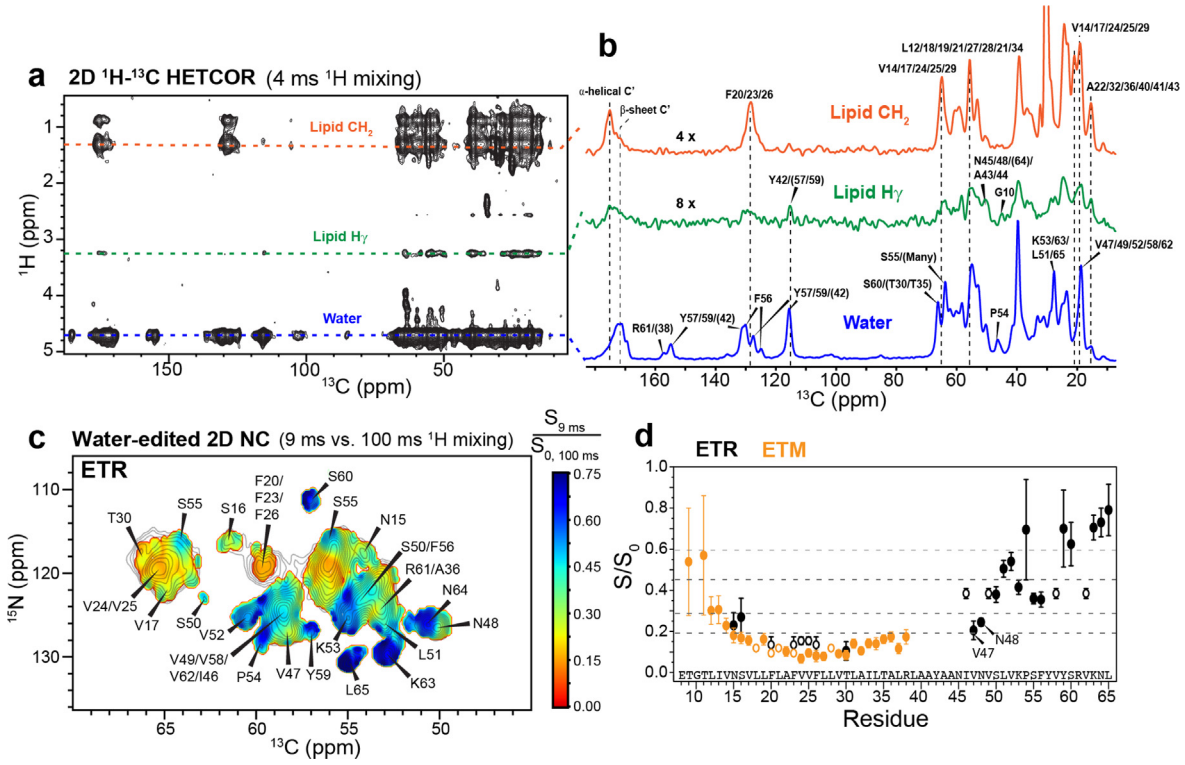

Figure 5. Depth of insertion and water accessibility of DMPC:DMPG membrane-bound ETR. (a) 2D ^{1}H–^{13}C HETCOR spectrum measured with 4 ms ^{1}H mixing. (b) 1D cross sections of the HETCOR spectrum at the lipid CH_2, headgroup Hγ, and water ^{1}H chemical shifts. These cross sections show the signals of deeply inserted residues, membrane-surface residues, and water accessible residues, respectively. (c) Water-edited 2D NC spectrum. Contour levels represent the intensity ratios of spectra measured with 9 ms (S) and 100 ms (S_0) ^{1}H mixing. High intensities indicate high water accessibility. (d) Water-transferred intensities of ETR versus ETM. Closed and open symbols indicate resolved and overlapping peaks, respectively.

residues.[41,42] The 2D NC spectrum has higher site resolution than the 2D CC spectrum, and detects water magnetization transfer to amide protons, which is independent of the presence or absence of exchangeable protons in the amino acid side-chains. Thus, the 2D NC spectrum is advantageous over the 2D CC spectrum for the water accessibility analysis. Two water-edited NC spectra were measured, using 9 ms and 100 ms ^{1}H mixing. Their intensity ratios represent the relative water accessibility of the amide protons. Well hydrated residues show high intensities in the 9 ms spectrum whereas dry residues exhibit low intensities. Figure 5(d) shows that residues in the middle of the TM domain display low water-transferred intensities whereas β-sheet signals have high water-edited intensities. Among the CTD residues, V47 and N48 have the lowest hydration, comparable to the water accessibility of TM residues, indicating that this portion of the CTD is shielded from water. This result is consistent with the close contact of ^{47}VNVSL^{51} with the membrane surface Hγ.

To obtain information about the three-dimensional fold of the CTD, we prepared a 1:1

Figure 6. Long-range intramolecular and intermolecular contacts of ETR. (a) NHHC spectrum of mixed ^{13}C-labeled ETR and ^{15}N-labeled ETR. All contacts are intermolecular. Selected assignments are indicated. (b) Region of the 250 ms 2D CC spectra of uniformly ^{13}C-labeled ETR and 50% diluted ^{13}C-labeled sample. Intermolecular contacts should decrease in relative intensity by 2-fold upon dilution (red assignment), while intramolecular contacts do not decrease in intensity (blue assignment). Dashed circles indicate S60-L51 cross peaks, which are more apparent in the diluted spectra due to increased signal averaging, and which are assigned to intramolecular contacts. (c) 2D cross sections of the 250 ms 3D CCC spectrum. Magenta assignments indicate long-range cross peaks. S55-I46/N64 and N48-S55 contacts are observed, which could be either intramolecular or intermolecular. (d) A representative cross section of the 250 ms 3D NCACX spectrum. A V47-V62/K63 correlation is observed (magenta assignment), which could be either intramolecular or intermolecular.

mixture of ^{13}C-labeled ETR and ^{15}N-labeled ETR, and measured its 2D NHHC spectrum (Figure 6 (a)). Due to the mixed labeling, all correlation signals are intermolecular. We observed intermolecular contacts between S60 and S60, L65 and N64, and S60 and N48. The first two contacts indicate that the β3 strands of different subunits are in close proximity, thus β3 should reside near the C_5 symmetry axis of the pentamer. We assigned all peaks that could not correspond

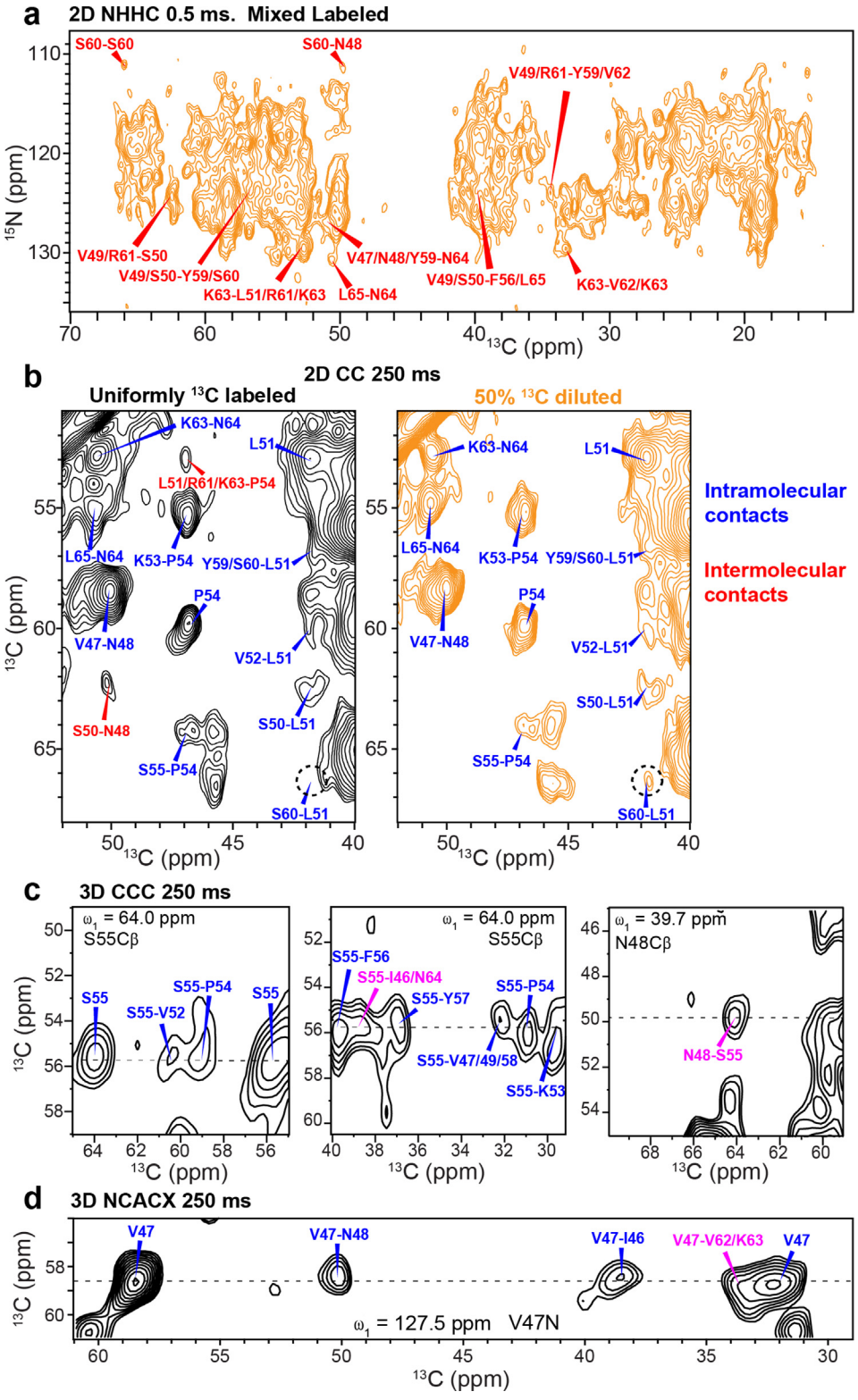

to the helical domain, and found 60 ambiguous contacts in addition to the 3 unambiguous contacts (Table S3, Table S4).

To supplement the NHHC data with additional intermolecular contacts, and to identify intramolecular long-range contacts, we measured 2D CC spectra with 250 ms ^{13}C spin diffusion (Figure 6(b)). The experiment was conducted on both uniformly ^{13}C, ^{15}N-labeled ETR and the 1:1 mixed labeled sample, where the ^{13}C-labeled ETR is diluted by an equal amount of unlabeled monomers. The two spectra are similar, except for a subset of peaks that disappeared in the diluted spectrum. These peaks include, for example, S50Cβ-N48Cα and L51/R61/K63Cα-P54Cδ. Due to the two-fold dilution, the intensities of purely intermolecular peaks are attenuated by 50%, while purely intramolecular peaks do not change intensity. Thus, these two contacts are intermolecular. The S60Cβ-L51Cβ cross peaks become more apparent in the diluted spectrum. Accounting for signal averaging differences, this cross peak has identical intensity in the diluted and undiluted samples, and is thus intramolecular.

Due to resonance overlap, few of the contacts in these 2D CC spectra can be assigned unambiguously. We thus carried out additional 3D CCC and 3D NCACX experiments with 250 ms ^{13}C spin diffusion (Figure 6(c, d)). These spectra were measured on uniformly ^{13}C, ^{15}N-labeled ETR, so that the correlations can be either intramolecular or intermolecular. However, even with the additional spectral dimension, resonance overlap persists among the CTD residues and between CTD and TM residues, which precluded unambiguous assignment of many cross peaks. In total, we observed 191 inter-residue correlations for CTD residues, among which 85 can be unambiguously assigned (Table S3, Table S4). For intermolecular contacts, there is a two-fold ambiguity about which of the two neighboring monomers is in close contact with the central monomer. These multiple possibilities are taken into account in the structure calculation of membrane-bound ETR.

Structural modeling of ETR cytoplasmic domain

We modeled the membrane-bound structure of the CTD in XPLOR-NIH[50] using 48 (ϕ, ψ) chemical-shift derived torsion angle restraints and 191 inter-residue distance restraints per monomer.[14] To maintain the proper topology with respect to the TM domain, we also included 32 NHHC intermolecular restraints for the TM domain obtained from the previous study of ETM.[18] We found that these restraints were insufficient to converge the simulated annealing to a single structure for residues 45–65. Instead, 78 of the lowest-energy 100 structures, including all of the 20 lowest energy structures, converged to one of four topologies (Figure 7). In all models, the CTD exhibits three β-strands that span approximately N45-V52, S55-V58 and R61-N64 (Figure 7(a)). While chemical shifts clearly indicate three β-strands, simulated annealing did not find hydrogen bonds for these β-strands, likely due to an insufficient number of long-range contacts. These cytoplasmic β-strands are connected to the TM domain by a linker at residues 37–44. The linker structure is poorly defined in the models due to low spectral intensities of these residues, suggesting that the linker is dynamically disordered. In all models, β1 and β2 strands are antiparallel, separated by a turn around K53-P54. β2 is followed by a turn into the radial center of the pentamer around S60, with the short β3 strand contacting β3 from other monomers and projecting in one of four directions. The four topologies in the 20 lowest energy structures differ by the orientations of the three β-strands: β1 proceeds down from the TM domain to either the left or the right; β2 is always above and antiparallel to β1; β3 proceeds radially inwards, but can point either up toward the TM domain or down toward the cytoplasm (Figure 7 (b, c)). Specifically, topology 1 has a left–right-up left (L-R-uL) displacement for the three β-strands, topology 2 L-R-dL, topology 3 L-R-uR, and topology 4 R-L-dL. These four topologies represent 36, 19, 11 and 12 models among the top 100 structures. Among the 20 lowest energy models, 15 models point β3 towards the membrane (topologies 1 and 3) while 5 models point the β3 strand down toward the cytoplasm (topologies 2 and 4). The two most prevalent topologies, 1 and 2, are nearly identical, except for whether β3 is pointed up towards the membrane or down towards the solvent. Since the β3 strand is highly water accessible (Figure 8(a)), the second topology is more probable than the first while the fourth topology is more probable than the third. Indeed, hydration surface plots (Figure 8) indicate that the second topology agrees with the water-edited data better than the first topology. The lower likelihood of the first and third topologies is also consistent with the fact that the C-terminus of full-length E contains a PDZ-binding motif that interacts with host proteins. Sequestering the β3 residues near the membrane surface is unlikely to expose the C-terminus of full-length E to the protein surface. We also depicted the membrane-surface Hγ-proximal residues in surface plots (Figure 8). These residues include G10, V12, and ^{42}YAAN^{45} in the linker between the TM and CTD domains, and are satisfied in all four topologies.

Discussion

Helix-sheet conformational difference of the E CTD

These solid-state NMR data show that the CTD of the SARS-CoV-2 E protein adopts a β-sheet rich conformation when bound to lipid bilayers at P/L ratios ranging from 1:20 to 1:60. This β-sheet

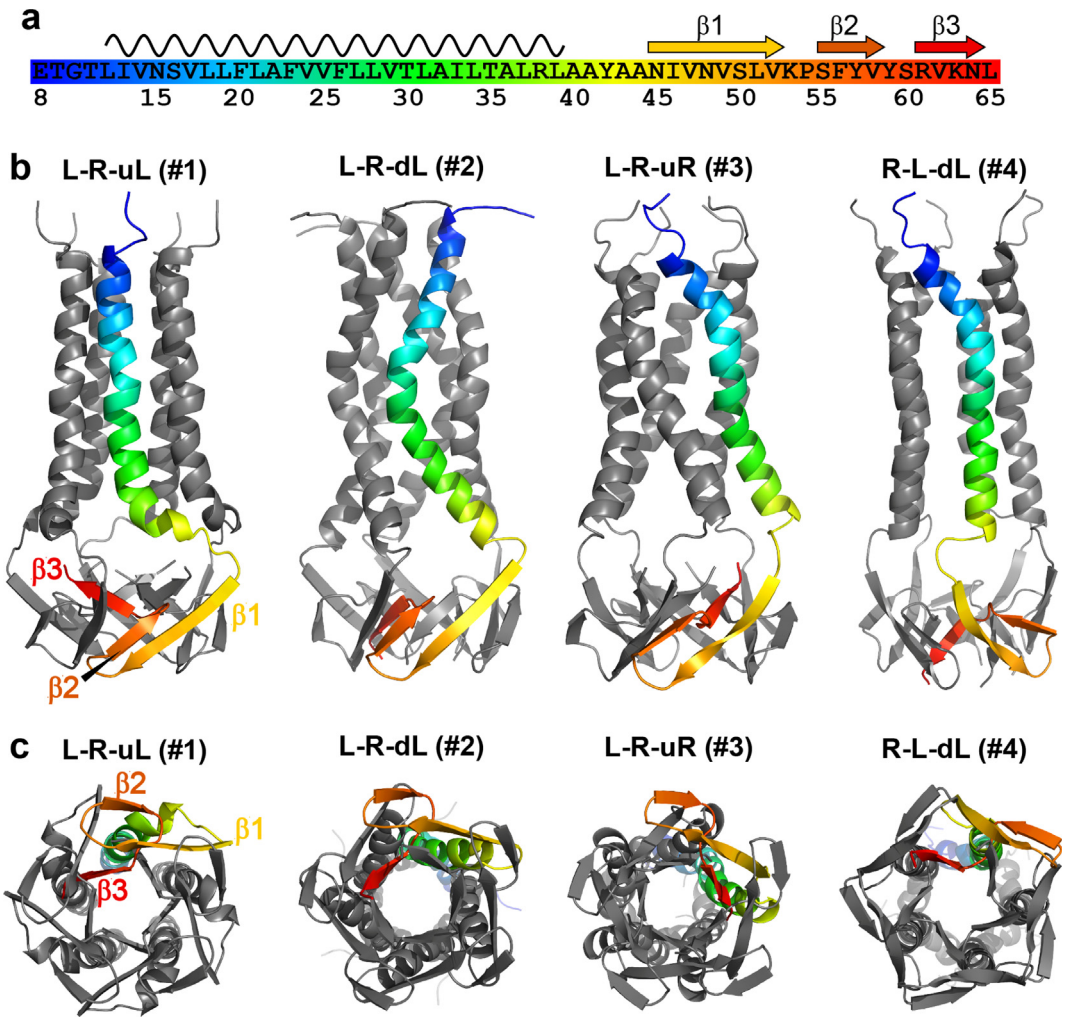

Figure 7. Range of structural models for the cytoplasmic domain of SARS-CoV-2 E in lipid bilayers. (a) Amino acid sequence of ETR, with secondary structures and color schemes indicated. (b, c) Four structural topologies of ETR obtained from simulated annealing. (b) Side views. (c) Views from the C-terminus. The NMR data do not uniquely constrain a structure, instead agree with four topologies for the cytoplasmic domain. The water accessibility of the C-terminal residues makes the first and third topologies less likely, as the C-terminus is hidden in the β-bundle, pointing towards the TM helices. We expect the true structure to be similar to one of these models, but unlike these models should have β-sheet hydrogen bonding. The helical TM domain is shown here only for context, and its structure varied widely in the simulated annealing. The variations among these models should only be considered for the cytoplasmic domain.

conformation is observed in both DMPC: DMPG membranes and in cholesterol-containing ERGIG-mimetic membranes. This β-rich conformation differs qualitatively from the α-helical conformation found in detergent micelles and at low protein concentrations in lipid bilayers.[10,28,29] Several factors could affect the secondary structure of the CTD: the lipid headgroup charge, the protein concentration, and the membrane curvature. We observed this β-sheet conformation in lipid bilayers containing 20–24 mol% negatively charged lipids, including DMPG, POPS and PI. This negative charge density is similar to that of eukaryotic membranes.[53] Solution NMR data showed that the CTD adopts α-helical conformation in a wide range of detergents, from negatively charged SDS and LMPG to neutral HPC.[29] A mixed detergent of DPC: SDS (4: 1) mixture[10,28] was also used, which has the same charge density as the DMPC: DMPG (4:1) membrane used here. An α-helical CTD was also observed in this mixed detergent. Thus, the β-sheet conformation in the current phospholipid bilayers cannot be attributed to different electrostatic interactions between the micelle samples and the membrane samples.

Instead, we attribute the β-sheet conformation to a combination of high protein concentration, low membrane curvature, and the amino acid sequence of this domain. The α-helical CTD is so far only observed at low P/L ratios and low

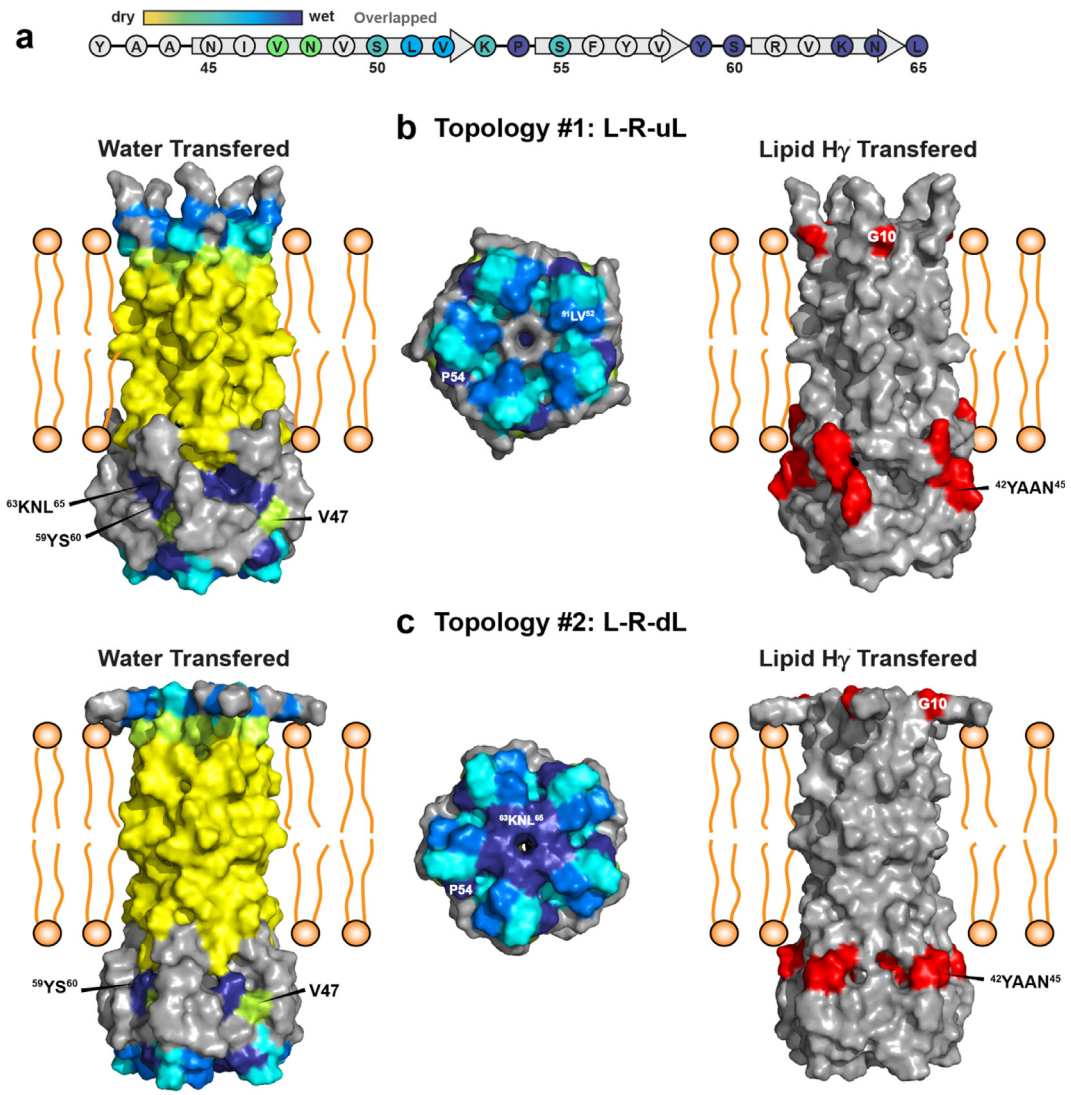

Figure 8. Water accessible and membrane-surface Hγ accessible residues in ETR. (a) Relative water accessibility of the cytoplasmic residues based on the water-edited spectra. The N-terminal portion of the CTD is less hydrated than the C-terminal portion. (b, c) Water (left and middle columns) and Hγ (right column) surface plots of the first and second topologies of ETR. Hγ-proximal residues, including G10 and linker residues ^{42}YAAN^{45}, are shown in red. (b) In topology 1, the C-terminal ^{63}KNL^{65} residues are occluded in the center of the β-bundle, inconsistent with the water-edited data. (c) In topology 2, the C-terminal residues are exposed to the solvent on the bottom surface of the β-bundle, thus this model agrees with the water-edited spectra. The hydration of residues 8–38 in ETR is represented by the water-edited data of ETM, which has similar hydration as ETR for these TM residues.

protein/detergent (P/D) molar ratios of less than 1:100.[10,28,29] A recent FT-IR study of ETR in the ERGIC membrane and the POPC: POPG membrane showed a β-sheet amide I peak (1632 cm^{-1}) at P/L 1:20, which disappears at lower P/L values of 1:100 and 1:400.[15] In C14 betaine micelles, ETR forms pentamers at a high P/D of 1:25 but monomers at a low P/D of 1:250. Thus, high protein concentrations both promote the pentamer state and the β-sheet conformation in lipid bilayers. In comparison, it has not been shown whether the α-helical conformation at low P/L ratios is associated with monomers or pentamers. But since E functions as a viroporin, we hypothesize that it retains the pentamer stoichiometry in lipid bilayers even at low protein concentrations. Sedimentation equilibrium data of full-length E in C14 betaine yielded a dissociation constant of P/D 1:83. Helix-helix interactions are known to be stronger in lipid bilayers than in detergent micelles.[54] Thus the dissociation constant is expected to be lower (i.e. smaller P/L values). Thus, the α-helical conformation seen at low P/L ratios in the FT-IR data may be associated with the pentamer state. At high P/L ratios of ~1:20, recent ^{19}F ssNMR data of ETM revealed clustering of the pentamers in

phosphatidylinositol (PI)-containing membranes. This clustering is manifested by the decay of the ^{19}F spin diffusion equilibrium intensity below the value of 0.20 expected for a pentamer.[14] This pentamer clustering implies that the local concentration of the E protein in the ERGIC membrane is higher than predicted by the P/L ratio. This high local concentration may promote the β-sheet conformation of the CTD by virtue of its compact shape.[15]

While the E concentration affects the CTD conformation,[15] the data shown here and in the literature so far do not exclude the possibility that the membrane curvature also contributes to the cytoplasmic conformation. All solution NMR studies that reported an α-helical CTD were conducted in high-curvature detergent micelles, whereas all ss-NMR and FT-IR studies that reported a β-sheet CTD were conducted in low-curvature lipid bilayers. Whether the CTD adopts an α-helical conformation in high-curvature lipid bilayers will require future investigation.

Apart from the environmental effects of protein concentration and membrane curvature, the amino acid sequence of the CTD encodes for a β-sheet propensity. A Val and Tyr-rich nine-residue peptide, ^{55}TVYVYSRVK^{63}, forms amyloid fibrils in solution.[31] Similar peptides (residues 46–60 and 36–76) in DMPC bilayers show β-sheet signals in FT-IR spectra[30] but α-helical signals in detergents.[55] The ^{56}XYVY^{59} motif within this nine-residue segment is also present in other coronavirus E proteins, and has been shown to form β-strand conformation.[10,56] Mutation of ^{56}XYVY^{59} to Ala abolished the β-sheet signals.[10] We hypothesize that the conformational plasticity of this nine-residue segment may be promoted by the coexistence of β-branched Val's (Val58 and Val62), aromatic residues (Tyr57, Tyr59), and cationic residues (Arg61 and Lys63), all of which can interact with negatively charged membrane surfaces through electrostatic as well as hydrophobic interactions. In this way, the local membrane curvature and the membrane surface charge may contribute to the conformational equilibrium of the CTD.

How would the helix-sheet conformational equilibrium of the CTD support the function of E? The number of E proteins in each virion varies considerably among different coronaviruses. Estimates range from 15-30 for the α-CoV transmissible gastroenteritis virus[57] to ∼100 for the γ-CoV infectious bronchitis virus.[58] In infected cell membranes, the E protein is believed to be present at higher concentrations, as it interacts with the M, S, and the nucleocapsid (N) proteins to modulate the cell secretory pathway, S maturation, and production of virus-like particles.[59] We hypothesize that the β-sheet CTD conformation may be operative when E is present abundantly in the low-curvature ERGIC membrane (Figure 9) where the β-sheet CTD interacts with the other virus proteins and with host proteins. When a new SARS-CoV-2 virus is ready to bud into the ERGIC lumen, sequestering a small number of E proteins into the virion envelope, we hypothesize that the high membrane curva-

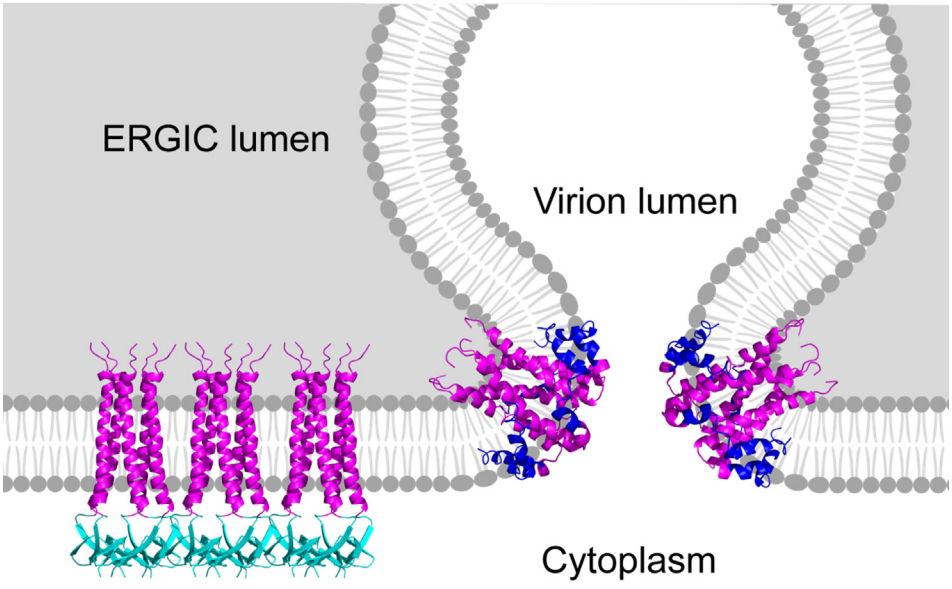

Figure 9. Proposed model of the locations of the SARS-CoV-2 E protein with β-sheet and α-helical cytoplasmic conformations. The β-sheet cytoplasmic conformation might exist in low-curvature ERGIC membranes where the E concentration is high. Here E may interact with M and S proteins to modulate the cell secretory pathway and mediate virus assembly and budding. The α-helical cytoplasmic conformation might occur in the high-curvature neck of the budding virus or the high-curvature virion envelope, where the E concentration is low. Here the amphipathic helix in the cytoplasmic domain might generate and/or sense negative Gaussian curvature.

ture at the neck of the budding virus may shift the CTD to the α-helical conformation. This hypothesis is made by analogy with the influenza viroporin M2, which possesses an amphipathic helix C-terminal to the TM domain.[60] This amphipathic helix mediates membrane scission in the last step of the influenza virus budding, by causing membrane curvature in a cholesterol-dependent manner.[61–63] Mutation of aromatic residues in this amphipathic helix inhibits membrane scission and influenza virus release. Assuming that the α-helical CTD of SARS-CoV-2 E observed at low concentrations in lipid bilayers is associated with pentamers, then an amphipathic helical domain in E may similarly mediate SARS-CoV-2 budding, by inducing and sensing membrane curvature at the neck of the budding virus.

Interestingly, the structure of the membrane protein M of the SARS-CoV-2 virus was recently solved and found to exhibit a cytoplasmic β-sheet sandwich that connects with the TM helices.[64,65] Although M is much larger than E and is dimeric instead of pentameric, its β-sheet cytoplasmic shape is similar to the E CTD conformation. In infectious bronchitis virus and SARS-CoV, M and E proteins are known to interact through their cytoplasmic domains, and this interaction is important for the formation of virus-like particles.[66,67] We speculate that either the β-sheet CTD or the α-helical CTD of E interacts with the cytoplasmic domain of the M protein, and this M−E interaction may occur when both proteins are present at high copy numbers in the ERGIC membrane. Thus, the helix-sheet conformational equilibria of E CTD might be important for the multiple functions of E at different stages of the virus lifecycle, in membranes with different curvatures, and in contact with different proteins.

Comparison of SARS-CoV-2 E with other viroporins

The SARS-CoV-2 E protein is multi-functional and multi-domain, a characteristic that is reminiscent of the properties of other viroporins[68] such as influenza A M2 (AM2), HIV Vpu,[69,70] and hepatitis C virus p7.[71] Extensive high-resolution structural data[60,72–77] and biochemical data[78–80] showed that the TM domain of AM2 forms a four-helix bundle, whereas its cytoplasmic domain contains an amphipathic helix.[81–83] In cholesterol- and phosphoethanolamine-rich membranes, this cytoplasmic helix causes membrane curvature,[84–87] which interferes with binding of the antiviral drug amantadine to the TM pore.[88–95]

The cytoplasmic helix of influenza AM2 does not exhibit any β-sheet tendency, but other virus membrane proteins have been reported to undergo conformational changes in response to membrane curvature or to cause membrane curvature. In the trimeric PIV5 F protein, the C-terminal TM domain adopts an α-helical conformation in phosphatidylcholine and phosphatidylglycerol membranes. But in phosphatidylethanolamine membranes, the two termini of the TM domain convert to β-strands.[96,97] These β-strand segments increase the membrane curvature, dehydrate the membrane, and promote membrane fusion. The N-terminal fusion peptides of PIV5 and HIV gp41 also exhibit membrane-dependent conformations.[98–100] In cholesterol-rich lipid bilayers, they adopt β-sheet conformations while in detergents and non-cholesterol membranes they mainly adopt α-helical structures.[101,102] The β-sheet conformation of the HIV gp41 fusion peptide is associated with membrane-curvature generation and sensing.[103,104] For influenza M2, the proton channel activity and tetramerization are accomplished by the TM domain, while the membrane scission function is accomplished by the cytoplasmic domain. The latter contains a curvature-inducing amphipathic helix and a disordered tail.[61,94] The SARS-CoV-2 E protein has various similarities to these viral membrane proteins. Like the PIV5 fusion protein TM domain and the PIV5 and HIV fusion peptides, the E CTD can adopt both helical and sheet conformations depending on its membrane environment. Like M2, E is a homo-oligomeric single-pass TM viroporin, with the CTD containing both a structured portion and a disordered tail. Future studies are required to understand whether it is the α-helical or β-sheet conformation of the E CTD that causes membrane curvature, and if this conformational transition is a sensor or a cause of membrane curvature.

Declaration of Competing Interest

The authors declare that they have no known competing financial interests or personal relationships that could have appeared to influence the work reported in this paper.

CRediT authorship contribution statement

Aurelio J. Dregni: Formal analysis, Validation, Writing – review & editing. **Matthew J. McKay:** Investigation, Formal analysis, Writing – original draft. **Wahyu Surya:** Investigation. **Maria Queralt-Martin:** Investigation. **João Medeiros-Silva:** Formal analysis. **Harrison K. Wang:** Formal analysis. **Vicente Aguilella:** Investigation, Supervision. **Jaume Torres:** Investigation, Supervision. **Mei Hong:** Conceptualization, Validation, Writing – review & editing, Supervision, Project administration, Funding acquisition.

Acknowledgement

This work is supported by NIH grant GM088204 to M.H. The NMR experiments used equipment at the MIT-Harvard Center for Magnetic Resonance, which is

supported by the P41 grant GM132079. A.J.D. was partially supported by an NIH fellowship F31AG069418. J.M.-S. gratefully acknowledges a Rubicon Fellowship 452020132 supported by the Dutch Research Council (NWO). J.T. acknowledges support of Singapore MOE Tier 1 grant RG92/21. M.Q. M. and V.M.A. acknowledge support from the Government of Spain MCIN/AEI/https://doi.org/10.13039/501100011033 (project no. 2019-108434GB-I00 AEI/FEDER, UE and IJC2018-035283-I/AEI) and Universitat Jaume I (project no. UJI-A2020-21).

Appendix A. Supplementary material

Tables of detailed experimental parameters, assigned chemical shifts and internuclear correlations. Additional NMR spectra, structural topologies, and ETR purification results are also provided. Supplementary material to this article can be found online at https://doi.org/10.1016/j.jmb.2023.167966.

Received 9 November 2022;
Accepted 11 January 2023;
Available online 20 January 2023

Keywords:
solid-state NMR;
structure determination;
membrane curvature;
viroporin;
oligomerization

† These authors contributed equally to this work.

References

1. Schoeman, D., Fielding, B.C., (2019). Coronavirus envelope protein: current knowledge. *Virol. J.* **16**, 69.
2. Nieto-Torres, J.L., DeDiego, M.L., Álvarez, E., Jiménez-Guardeño, J.M., Regla-Nava, J.A., Llorente, M., et al., (2011). Subcellular location and topology of severe acute respiratory syndrome coronavirus envelope protein. *Virology* **415**, 69–82.
3. Torres, J., Maheswari, U., Parthasarathy, K., Ng, L., Liu, D.X., Gong, X., (2007). Conductance and amantadine binding of a pore formed by a lysine-flanked transmembrane domain of SARS coronavirus envelope protein. *Protein Sci.* **16**, 2065–2071.
4. Wilson, L., McKinlay, C., Gage, P., Ewart, G., (2004). SARS coronavirus E protein forms cation-selective ion channels. *Virology* **330**, 322–331.
5. Nieto-Torres, J.L., Verdiá-Báguena, C., Jimenez-Guardeño, J.M., Regla-Nava, J.A., Castaño-Rodriguez, C., Fernandez-Delgado, R., et al., (2015). Severe acute respiratory syndrome coronavirus E protein transports calcium ions and activates the NLRP3 inflammasome. *Virology* **485**, 330–339.
6. Nieto-Torres, J.L., DeDiego, M.L., Verdia-Baguena, C., Jimenez-Guardeno, J.M., Regla-Nava, J.A., Fernandez-Delgado, R., et al., (2014). Severe acute respiratory syndrome coronavirus envelope protein ion channel activity promotes virus fitness and pathogenesis. *PLoS Pathog.* **10**, e1004077.
7. Verdia-Baguena, C., Nieto-Torres, J.L., Alcaraz, A., Dediego, M.L., Enjuanes, L., Aguilella, V.M., (2013). Analysis of SARS-CoV E protein ion channel activity by tuning the protein and lipid charge. *BBA* **1828**, 2026–2031.
8. Verdiá-Báguena, C., Nieto-Torres, J.L., Alcaraz, A., DeDiego, M.L., Torres, J., Aguilella, V.M., et al., (2012). Coronavirus E protein forms ion channels with functionally and structurally-involved membrane lipids. *Virology* **432**, 485–494.
9. Parthasarathy, K., Ng, L., Lin, X., Liu, D.X., Pervushin, K., Gong, X., et al., (2008). Structural flexibility of the pentameric SARS coronavirus envelope protein ion channel. *Biophys. J.* **95**, L39–L41.
10. Li, Y., Surya, W., Claudine, S., Torres, J., (2014). Structure of a conserved Golgi complex-targeting signal in coronavirus envelope proteins. *J. Biol. Chem.* **289**, 12535–12549.
11. Parthasarathy, K., Lu, H., Surya, W., Vararattanavech, A., Pervushin, K., Torres, J., (2012). Expression and purification of coronavirus envelope proteins using a modified β-barrel construct. *Protein Expr. Purif.* **85**, 133–141.
12. Appenzeller-Herzog, C., Hauri, H.P., (2006). The ER-Golgi intermediate compartment (ERGIC): in search of its identity and function. *J. Cell Sci.* **119**, 2173–2183.
13. Murakami, T., Ockinger, J., Yu, J., Byles, V., McColl, A., Hofer, A.M., et al., (2012). Critical role for calcium mobilization in activation of the NLRP3 inflammasome. *PNAS* **109**, 11282–11287.
14. Somberg, N.H., Wu, W.W., Medeiros-Silva, J., Dregni, A. J., Jo, H., DeGrado, W.F., et al., (2022). SARS-CoV-2 Envelope Protein Forms Clustered Pentamers in Lipid Bilayers. *Biochemistry* **61**, 2280–2294.
15. Surya, W., Torres, J., (2022). Oligomerization-Dependent Beta-Structure Formation in SARS-CoV-2 Envelope Protein. *Int. J. Mol. Sci.* **23**, 13285.
16. Pervushin, K., Tan, E., Parthasarathy, K., Lin, X., Jiang, F. L., Yu, D., et al., (2009). Structure and Inhibition of the SARS Coronavirus Envelope Protein Ion Channel. *PLoS Pathog.* **5**
17. Torres, J., Parthasarathy, K., Lin, X., Saravanan, R., Kukol, A., Liu, D.X., (2006). Model of a putative pore: the pentameric alpha-helical bundle of SARS coronavirus E protein in lipid bilayers. *Biophys. J.* **91**, 938–947.
18. Mandala, V.S., McKay, M.J., Shcherbakov, A.A., Dregni, A.J., Kolocouris, A., Hong, M., (2020). Structure and drug binding of the SARS-CoV-2 envelope protein transmembrane domain in lipid bilayers. *Nature Struct. Mol. Biol.* **27**, 1202–1208.
19. Medeiros-Silva, J., Somberg, N.H., Wang, H.K., McKay, M.J., Mandala, V.S., Dregni, A.J., et al., (2022). pH- and Calcium-Dependent Aromatic Network in the SARS-CoV-2 Envelope Protein. *J. Am. Chem. Soc.* **144**, 6839–6850.
20. Teoh, K.T., Siu, Y.L., Chan, W.L., Schlüter, M.A., Liu, C. J., Peiris, J.S., et al., (2010). The SARS coronavirus E protein interacts with PALS1 and alters tight junction formation and epithelial morphogenesis. *Mol. Biol. Cell* **21**, 3838–3852.
21. Jimenez-Guardeño, J.M., Regla-Nava, J.A., Nieto-Torres, J.L., DeDiego, M.L., Castaño-Rodriguez, C., Fernandez-Delgado, R., et al., (2015). Identification of the

Mechanisms Causing Reversion to Virulence in an Attenuated SARS-CoV for the Design of a Genetically Stable Vaccine. *PLoS Pathog.* **11**, e1005215.
22. Toto, A., Ma, S., Malagrinò, F., Visconti, L., Pagano, L., Stromgaard, K., et al., (2020). Comparing the binding properties of peptides mimicking the Envelope protein of SARS-CoV and SARS-CoV-2 to the PDZ domain of the tight junction-associated PALS1 protein. *Protein Sci.* **29**, 2038–2042.
23. Javorsky, A., Humbert, P.O., Kvansakul, M., (2021). Structural basis of coronavirus E protein interactions with human PALS1 PDZ domain. *Commun. Biol.* **4**, 724.
24. Jose, R.J., Manuel, A., (2020). COVID-19 cytokine storm: the interplay between inflammation and coagulation. *Lancet Respir. Med.* **8**, e46–e47.
25. Zheng, M., Karki, R., Williams, E.P., Yang, D., Fitzpatrick, E., Vogel, P., et al., (2021). TLR2 senses the SARS-CoV-2 envelope protein to produce inflammatory cytokines. *Nature Immunol.* **22**, 829–838.
26. Ruch, T.R., Machamer, C.E., (2012). The coronavirus E protein: assembly and beyond. *Viruses* **4**, 363–382.
27. Regla-Nava, J.A., Nieto-Torres, J.L., Jimenez-Guardeño, J.M., Fernandez-Delgado, R., Fett, C., Castaño-Rodríguez, C., et al., (2015). Severe acute respiratory syndrome coronaviruses with mutations in the E protein are attenuated and promising vaccine candidates. *J. Virol.* **89**, 3870–3887.
28. Surya, W., Li, Y., Torres, J., (2018). Structural model of the SARS coronavirus E channel in LMPG micelles. *Biochim. Biophys. Acta Biomembr.* **1860**, 1309–1317.
29. Park, S.H., Siddiqi, H., Castro, D.V., De Angelis, A.A., Oom, A.L., Stoneham, C.A., et al., (2021). Interactions of SARS-CoV-2 envelope protein with amilorides correlate with antiviral activity. *PLoS Pathog.* **17**, e1009519.
30. Surya W, Samsó M, Torres J. Structural and Functional Aspects of Viroporins in Human Respiratory Viruses: Respiratory Syncytial Virus and Coronaviruses. In: Vats M, editor. Respiratory Disease and Infection – A New Insight2013.
31. Ghosh, A., Pithadia, A.S., Bhat, J., Bera, S., Midya, A., Fierke, C.A., et al., (2015). Self-Assembly of a Nine-Residue Amyloid-Forming Peptide Fragment of SARS Corona Virus E-Protein: Mechanism of Self Aggregation and Amyloid-Inhibition of hIAPP. *Biochemistry* **54**, 2249–2261.
32. Savitsky, P., Bray, J., Cooper, C.D., Marsden, B.D., Mahajan, P., Burgess-Brown, N.A., et al., (2010). High-throughput production of human proteins for crystallization: the SGC experience. *J. Struct. Biol.* **172**, 3–13.
33. Studier, F.W., (2014). Stable Expression Clones and Auto-Induction for Protein Production in E. coli. In: Chen, Y.W. (Ed.), *Structural Genomics: General Applications*. Humana Press, Totowa, NJ, pp. 17–32.
34. Sivashanmugam, A., Murray, V., Cui, C.X., Zhang, Y.H., Wang, J.J., Li, Q.Q., (2009). Practical protocols for production of very high yields of recombinant proteins using Escherichia coli. *Protein Sci.* **18**, 936–948.
35. Bezrukov, S.M., Vodyanoy, I., (1993). Probing alamethicin channels with water-soluble polymers. Effect on conductance of channel states. *Biophys. J.* **64**, 16–25.
36. Montal, M., Mueller, P., (1972). Formation of bimolecular membranes from lipid monolayers and a study of their electrical properties. *PNAS* **69**, 3561–3566.
37. Böckmann, A., Gardiennet, C., Verel, R., Hunkeler, A., Loquet, A., Pintacuda, G., et al., (2009). Characterization of different water pools in solid-state NMR protein samples. *J. Biomol. NMR* **45**, 319–327.
38. Hou, G.J., Yan, S., Trebosc, J., Amoureux, J.P., Polenova, T., (2013). Broadband homonuclear correlation spectroscopy driven by combined R2(n)(ν) sequences under fast magic angle spinning for NMR structural analysis of organic and biological solids. *J. Magn. Reson.* **232**, 18–30.
39. Rienstra, C.M., Hohwy, M., Hong, M., Griffin, R.G., (2000). 2D and 3D 15N–13C–13C NMR Chemical Shift Correlation Spectroscopy of Solids: Assignment of MAS Spectra of Peptides. *J. Am. Chem. Soc.* **122**, 10979–10990.
40. Baldus, M., Petkova, A.T., Herzfeld, J., Griffin, R.G., (1998). Cross polarization in the tilted frame: assignment and spectral simplification in heteronuclear spin systems. *Mol. Phys.* **95**, 1197–1207.
41. Williams, J.K., Hong, M., (2014). Probing membrane protein structure using water polarization transfer solid-state NMR. *J. Magn. Reson.* **247**, 118–127.
42. Dregni, A.J., Duan, P., Hong, M., (2020). Hydration and Dynamics of Full-Length Tau Amyloid Fibrils Investigated by Solid-State Nuclear Magnetic Resonance. *Biochemistry* **59**, 2237–2248.
43. Caravatti, P., Braunschweiler, L., Ernst, R.R., (1983). Heteronuclear correlation spectroscopy in rotating solids. *Chem. Phys. Lett.* **100**, 305–310.
44. Roberts, J.E., Vega, S., Griffin, R.G., (1984). Two-dimensional heteronuclear chemical shift correlation spectroscopy in rotating solids. *J. Am. Chem. Soc.* **106**, 2506–2512.
45. Lange, A., Luca, S., Baldus, M., (2002). Structural Constraints from Proton-Mediated Rare-Spin Correlation Spectroscopy in Rotating Solids. *J. Am. Chem. Soc.* **124**, 9704–9705.
46. Goddard TD, Kneller DG. SPARKY 3. University of California, San Francisco.
47. Shen, Y., Bax, A., (2013). Protein backbone and sidechain torsion angles predicted from NMR chemical shifts using artificial neural networks. *J. Biomol. NMR* **56**, 227–241.
48. Mandala, V.S., Loftis, A.R., Shcherbakov, A.A., Pentelute, B.L., Hong, M., (2020). Atomic structures of closed and open influenza B M2 proton channel reveal the conduction mechanism. *Nature Struct. Mol. Biol.* **27**, 160–167.
49. Helmus, J.J., Jaroniec, C.P., (2013). Nmrglue: an open source Python package for the analysis of multidimensional NMR data. *J. Biomol. NMR* **55**, 355–367.
50. Schwieters, C.D., Kuszewski, J.J., Tjandra, N., Clore, G. M., (2003). The Xplor-NIH NMR molecular structure determination package. *J. Magn. Reson.* **160**, 65–73.
51. Maciejewski, M.W., Schuyler, A.D., Gryk, M.R., Moraru, I. I., Romero, P.R., Ulrich, E.L., et al., (2017). NMRbox: A Resource for Biomolecular NMR Computation. *Biophys. J.* **112**, 1529–1534.
52. Huster, D., Yao, X.L., Hong, M., (2002). Membrane Protein Topology Probed by 1H Spin Diffusion from Lipids Using Solid-State NMR Spectroscopy. *J. Am. Chem. Soc.* **124**, 874–883.
53. van Meer, G., Voelker, D.R., Feigenson, G.W., (2008). Membrane lipids: where they are and how they behave. *Nature Rev. Mol. Cell Biol.* **9**, 112–124.

54. Stouffer, A.L., Ma, C., Cristian, L., Ohigashi, Y., Lamb, R. A., Lear, J.D., et al., (2008). The interplay of functional tuning, drug resistance, and thermodynamic stability in the evolution of the M2 proton channel from the influenza A virus. *Structure*, 1067–1076.
55. Ghosh, A., Bhattacharyya, D., Bhunia, A., (2018). Structural insights of a self-assembling 9-residue peptide from the C-terminal tail of the SARS corona virus E-protein in DPC and SDS micelles: A combined high and low resolution spectroscopic study. *Biochim. Biophys. Acta Biomembr.* **1860**, 335–346.
56. Combet, C., Blanchet, C., Geourjon, C., Deléage, G., (2000). NPS@: network protein sequence analysis. *Trends Biochem. Sci.* **25**, 147–150.
57. Godet, M., L'Haridon, R., Vautherot, J.F., Laude, H., (1992). TGEV corona virus ORF4 encodes a membrane protein that is incorporated into virions. *Virology* **188**, 666–675.
58. Liu, D.X., Inglis, S.C., (1991). Association of the infectious bronchitis virus 3c protein with the virion envelope. *Virology* **185**, 911–917.
59. Boson, B., Legros, V., Zhou, B., Siret, E., Mathieu, C., Cosset, F.L., et al., (2021). The SARS-CoV-2 envelope and membrane proteins modulate maturation and retention of the spike protein, allowing assembly of virus-like particles. *J. Biol. Chem.* **296**, 100111
60. Sharma, M., Yi, M., Dong, H., Qin, H., Peterson, E., Busath, D.D., et al., (2010). Insight into the mechanism of the influenza A proton channel from a structure in a lipid bilayer. *Science* **330**, 509–512.
61. Rossman, J.S., Jing, X.H., Leser, G.P., Lamb, R.A., (2010). Influenza Virus M2 Protein Mediates ESCRT-Independent Membrane Scission. *Cell* **142**, 902–913.
62. Elkins, M.R., Williams, J.K., Gelenter, M.D., Dai, P., Kwon, B., Sergeyev, I.V., et al., (2017). Cholesterol-binding site of the influenza M2 protein in lipid bilayers from solid-state NMR. *PNAS* **114**, 12946–12951.
63. Elkins, M.R., Sergeyev, I.V., Hong, M., (2018). Determining Cholesterol Binding to Membrane Proteins by Cholesterol 13C Labeling in Yeast and Dynamic Nuclear Polarization NMR. *J. Am. Chem. Soc.* **140**, 15437–15449.
64. Zhang, Z., Nomura, N., Muramoto, Y., Ekimoto, T., Uemura, T., Liu, K., et al., (2022). Structure of SARS-CoV-2 membrane protein essential for virus assembly. *Nature Commun.* **13**, 4399.
65. Dolan, K.A., Dutta, M., Kern, D.M., Kotecha, A., Voth, G. A., Brohawn, S.G., (2022). Structure of SARS-CoV-2 M protein in lipid nanodiscs. *Elife* **11**
66. Corse, E., Machamer, C.E., (2003). The cytoplasmic tails of infectious bronchitis virus E and M proteins mediate their interaction. *Virology* **312**, 25–34.
67. Mortola, E., Roy, P., (2004). Efficient assembly and release of SARS coronavirus-like particles by a heterologous expression system. *FEBS Lett.* **576**, 174–178.
68. Nieva, J.L., Madan, V., Carrasco, L., (2012). Viroporins: structure and biological functions. *Nature Rev. Microbiol.* **10**, 563–574.
69. Park, S.H., Mrse, A.A., Nevzorov, A.A., Mesleh, M.F., Oblatt-Montal, M., Montal, M., et al., (2003). Three-dimensional structure of the channel-forming trans-membrane domain of virus protein "u" (Vpu) from HIV-1. *J. Mol. Biol.* **333**, 409–424.
70. Lu, J.X., Sharpe, S., Ghirlando, R., Yau, W.M., Tycko, R., (2010). Oligomerization state and supramolecular structure of the HIV-1 Vpu protein transmembrane segment in phospholipid bilayers. *Protein Sci.*.
71. OuYang, B., Xie, S., Berardi, M.J., Zhao, X., Dev, J., Yu, W., et al., (2013). Unusual architecture of the p7 channel from hepatitis C virus. *Nature* **498**, 521–525.
72. Hong, M., DeGrado, W.F., (2012). Structural basis for proton conduction and inhibition by the influenza M2 protein. *Prot. Sci.* **21**, 1620–1633.
73. Hu, F., Schmidt-Rohr, K., Hong, M., (2012). NMR detection of pH-dependent histidine-water proton exchange reveals the conduction mechanism of a transmembrane proton channel. *J. Am. Chem. Soc.* **134**, 3703–3713.
74. Acharya, A., Carnevale, V., Fiorin, G., Levine, B.G., Polishchuk, A., Balannick, V., et al., (2010). Structural mechanism of proton transport through the influenza A M2 protein. *PNAS* **107**, 15075–15080.
75. Thomaston, J.L., Alfonso-Prieto, M., Woldeyes, R.A., Fraser, J.S., Klein, M.L., Fiorin, G., et al., (2015). High-resolution structures of the M2 channel from influenza A virus reveal dynamic pathways for proton stabilization and transduction. *PNAS* **112**, 14260–14265.
76. Cady, S.D., Hong, M., (2008). Amantadine-Induced Conformational and Dynamical Changes of the Influenza M2 Transmembrane Proton Channel. *PNAS* **105**, 1483–1488.
77. Mandala, V.S., Liao, S.Y., Kwon, B., Hong, M., (2017). Structural Basis for Asymmetric Conductance of the Influenza M2 Proton Channel Investigated by Solid-State NMR Spectroscopy. *J. Mol. Biol.* **429**, 2192–2210.
78. Pinto, L.H., Holsinger, L.J., Lamb, R.A., (1992). Influenza virus M2 protein has ion channel activity. *Cell* **69**, 517–528.
79. Balannik, V., Carnevale, V., Fiorin, G., Levine, B.G., Lamb, R.A., Klein, M.L., et al., (2010). Functional studies and modeling of pore-lining residue mutants of the influenza a virus M2 ion channel. *Biochemistry* **49**, 696–708.
80. Pinto, L.H., Lamb, R.A., (2006). The M2 proton channels of influenza A and B viruses. *J. Biol. Chem.* **281**, 8997–9000.
81. Huang, S., Green, B., Thompson, M., Chen, R., Thomaston, J., DeGrado, W.F., et al., (2015). C-terminal juxtamembrane region of full-length M2 protein forms a membrane surface associated amphipathic helix. *Protein Sci.* **24**, 426–429.
82. Kim, S.S., Upshur, M.A., Saotome, K., Sahu, I.D., McCarrick, R.M., Feix, J.B., et al., (2015). Cholesterol-Dependent Conformational Exchange of the C-Terminal Domain of the Influenza A M2 Protein. *Biochemistry* **54**, 7157–7167.
83. Tian, C., Gao, P.F., Pinto, L.H., Lamb, R.A., Cross, T.A., (2003). Initial structural and dynamic characterization of the M2 protein transmembrane and amphipathic helices in lipid bilayers. *Protein Sci.* **12**, 2597–2605.
84. Cady, S., Wang, T., Hong, M., (2011). Membrane-Dependent Effects of a Cytoplasmic Helix on the Structure and Drug Binding of the Influenza Virus M2 Protein. *J. Am. Chem. Soc.* **133**, 11572–11579.
85. Wang, T., Hong, M., (2015). Investigation of the Curvature Induction and Membrane Localization of the Influenza Virus M2 Protein Using Static and Off-Magic-Angle-

Spinning Solid-State Nuclear Magnetic Resonance of Oriented Bicelles. *Biochemistry* **54**, 2214–2226.
86. Schmidt, N.W., Mishra, A., Wang, J., DeGrado, W.F., Wong, G.C.L., (2013). Influenza Virus A M2 Protein Generates Negative Gaussian Membrane Curvature Necessary for Budding and Scission. *J. Am. Chem. Soc.* **135**, 13710–13719.
87. Kim, G., Raymond, H.E., Herneisen, A.L., Wong-Rolle, A., Howard, K.P., (2019). The distal cytoplasmic tail of the influenza A M2 protein dynamically extends from the membrane. *BBA* **1861**, 1421–1427.
88. Cady, S.D., Schmidt-Rohr, K., Wang, J., Soto, C.S., Degrado, W.F., Hong, M., (2010). Structure of the amantadine binding site of influenza M2 proton channels in lipid bilayers. *Nature* **463**, 689–692.
89. Stouffer, A.L., Acharya, R., Salom, D., Levine, A.S., Di Costanzo, L., Soto, C.S., et al., (2008). Structural basis for the function and inhibition of an influenza virus proton channel. *Nature* **451**, 596–599.
90. Wang, J., Ma, C., Fiorin, G., Carnevale, V., Wang, T., Hu, F., et al., (2011). Molecular dynamics simulation directed rational design of inhibitors targeting drug-resistant mutants of influenza A virus M2. *J. Am. Chem. Soc.* **133**, 12834–12841.
91. Wang, J., Wu, Y., Ma, C., Fiorin, G., Wang, J., Pinto, L.H., et al., (2013). Structure and inhibition of the drug-resistant S31N mutant of the M2 ion channel of influenza A virus. *PNAS* **110**, 1315–1320.
92. Andreas, L.B., Barnes, A.B., Corzilius, B., Chou, J.J., Miller, E.A., Caporini, M., et al., (2013). Dynamic nuclear polarization study of inhibitor binding to the M2(18–60) proton transporter from influenza A. *Biochemistry* **52**, 2774–2782.
93. Jing, X., Ma, C., Ohigashi, Y., Oliveira, F.A., Jardetzky, T. S., Pinto, L.H., et al., (2008). Functional studies indicate amantadine binds to the pore of the influenza A virus M2 proton-selective ion channel. *PNAS* **105**, 10967–10972.
94. Liao, S.Y., Lee, M., Hong, M., (2019). Interplay between membrane curvature and protein conformational equilibrium investigated by solid-state NMR. *J. Struct. Biol.* **206**, 20–28.
95. Pielak, R.M., Oxenoid, K., Chou, J.J., (2011). Structural investigation of rimantadine inhibition of the AM2-BM2 chimera channel of influenza viruses. *Structure* **19**, 1655–1663.
96. Lee, M., Yao, H., Kwon, B., Waring, A.J., Ruchala, P., Singh, C., et al., (2018). Conformation and Trimer Association of the Transmembrane Domain of the Parainfluenza Virus Fusion Protein in Lipid Bilayers from Solid-State NMR: Insights into the Sequence Determinants of Trimer Structure and Fusion Activity. *J. Mol. Biol.* **430**, 695–709.
97. Yao, H., Lee, M.W., Waring, A.J., Wong, G.C., Hong, M., (2015). Viral fusion protein transmembrane domain adopts beta-strand structure to facilitate membrane topological changes for virus-cell fusion. *PNAS* **112**, 10926–10931.
98. Rafalski, M., Lear, J.D., DeGrado, W.F., (1990). Phospholipid interactions of synthetic peptides representing the N-terminus of HIV gp41. *Biochemistry* **29**, 7917–7922.
99. Yang, J., Gabrys, C.M., Weliky, D.P., (2001). Solid-state nuclear magnetic resonance evidence for an extended beta strand conformation of the membrane-bound HIV-1 fusion peptide. *Biochemistry* **40**, 8126–8137.
100. Yang, J., Prorok, M., Castellino, F.J., Weliky, D.P., (2004). Oligomeric beta-structure of the membrane-bound HIV-1 fusion peptide formed from soluble monomers. *Biophys. J.* **87**, 1951–1963.
101. Yao, H., Hong, M., (2014). Conformation and Lipid Interaction of the Fusion Peptide of the Paramyxovirus PIV5 in Anionic and Negative-Curvature Membranes from Solid-State NMR. *J. Am. Chem. Soc.* **136**, 2611–2624.
102. Lai, A.L., Moorthy, A.E., Li, Y., Tamm, L.K., (2012). Fusion Activity of HIV gp41 Fusion Domain Is Related to Its Secondary Structure and Depth of Membrane Insertion in a Cholesterol-Dependent Fashion. *J. Mol. Biol.* **418**, 3–15.
103. Qiang, W., Sun, Y., Weliky, D.P., (2009). A strong correlation between fusogenicity and membrane insertion depth of the HIV fusion peptide. *PNAS* **106**, 15314–15319.
104. Qiang, W., Weliky, D.P., (2009). HIV fusion peptide and its cross-linked oligomers: efficient syntheses, significance of the trimer in fusion activity, correlation of beta strand conformation with membrane cholesterol, and proximity to lipid headgroups. *Biochemistry* **48**, 289–301.